Article

Bipolar junction transistor amplifiers-state-space modeling across frequencies

José M. Campos-Salazar[1],* ⓘ**, Juan L. Aguayo-Lazcano[2]** ⓘ**, Roya Rafiezadeh[3], and Gabriel García-Rojas[1]**

1 Electronic Engineering Department, Universitat Politècnica de Catalunya, Barcelona, España

2 Institute of Physical and Mathematical Sciences, Universidad Austral de Chile, Valdivia, Chile

3 The PEMC group, University of Nottingham, Nottingham, UK

* Correspondence: jose.manuel,campos@upc.edu

Abstract: This study presents a unified time-domain analysis of three fundamental bipolar-junction-transistor amplifier topologies—common-emitter (CEA), common-collector (CCA), and common-base (CBA)—under both low- and high-frequency transient conditions. Unlike traditional small-signal or SPICE-based approaches, this work employs a state-space modeling framework implemented in MATLAB-Simulink to derive and simulate the dynamic behavior of each topology. The models capture both steady-state and transient responses, offering deeper insight into system dynamics, including the effects of Miller capacitance at high frequencies. The CEA demonstrates high voltage gain, while the CCA and CBA exhibit lower but topology-consistent gains, with simulation results closely matching analytical predictions. Although experimental validation is not included, the simulation parameters are carefully selected to reflect realistic operating conditions. The novelty of this work lies in its application of state-space methods to analog amplifier modeling, providing a transparent and extendable foundation for analyzing more complex circuits such as operational amplifiers. This approach enhances theoretical understanding and supports practical design decisions across a wide range of analog applications.

Keywords: BJT amplifiers, low and high frequency operation, simulation modeling, transient's analysis, voltage gain characteristics

1. Introduction

The field of low-power signal amplification remains a cornerstone of analog microelectronics, especially in applications that require high performance over a wide range of frequencies. Among the active devices employed in amplification tasks, bipolar junction transistors (BJTs) continue to hold significance due to their intrinsic gain characteristics and well-understood behavior, despite the prevalent dominance of operational amplifiers (Op-Amps) in

contemporary analog circuit design [1–5]. While Op-Amps are favored for their ease of implementation and high input impedance, their limitations—particularly regarding output drive capabilities and frequency response linearity—make BJTs a competitive choice for precision and high-frequency analog applications [6,7].

Traditionally, the design and analysis of BJT-based amplifiers rely on small-signal models and hybrid-π equivalent circuits, typically analyzed in the frequency domain [8–11]. However, such methods often neglect time-domain characteristics essential for predicting transient responses, which are critical in many real-world signal-processing and communication systems. Furthermore, commercial circuit simulators such as LTspice and PSpice often employ black-box behavioral models that obscure the underlying physics and limit analytical insight. To address this gap, this work adopts a state-space modeling framework that captures the time-domain dynamics of BJT amplifier topologies under both low- and high-frequency conditions.

A robust understanding of the fundamental amplifier topologies—common-emitter (CEA), common-collector (CCA), and common-base (CBA)—is essential, as each configuration offers distinct advantages. The CEA is known for its high voltage gain and sensitivity to the Miller effect at high frequencies [12,13]. The CCA, or emitter follower, offers low output impedance and unity gain, making it ideal for impedance matching [14], while the CBA provides superior high-frequency performance due to its inherently low input impedance and minimal Miller capacitance influence [15].

Despite their ubiquity in electronics education and analog design, few studies present a unified time-domain modeling framework for these topologies that allows a direct comparison of their transient behaviors. Recent research [16–18] has explored variations in transistor-level behavior under non-ideal and high-frequency conditions, but these works often treat the amplifier configurations separately or focus exclusively on steady-state performance. This paper seeks to bridge that gap by developing and validating state-space models for the CEA, CCA, and CBA topologies that are valid across frequency domains.

The novelty of this work lies in its application of state-space modeling to analog amplifier circuits, enabling a dynamic, time-domain analysis that is both analytically and simulation-friendly. This approach not only enhances understanding of transient behavior but also lays the groundwork for modeling more complex analog systems, such as operational amplifiers, where internal stages often mirror the topologies studied here. By validating the models through MATLAB-Simulink simulations, the study offers a transparent and extendable framework that complements traditional SPICE-based tools and supports future integration into larger analog design workflows.

In this context, the manuscript is structured to reflect theoretical contributions. Section 2 outlines the topological structure and typical operating conditions of each amplifier configuration. Section 3 derives the complete state-space models, incorporating both linearized and nonlinear circuit elements. Section 4 presents the analytical solutions derived from these models. Section 5 validates these solutions through transient simulations using MATLAB-Simulink, comparing analytical results with numerical outputs to confirm model accuracy. Section 6 concludes the study by summarizing the key insights and discussing their implications for amplifier design and future extensions to more complex analog systems.

2. Amplifiers based on BJTs topologies

The foundational theory of BJT-based amplifiers encompasses three primary configurations, each optimized for specific performance metrics in analog signal processing: the CEA, the CCA, and the CBA [19,20]. Among them, the CEA is the most widely used due to its high voltage gain and moderate input impedance. The CCA, also known as the emitter follower, is commonly employed for impedance matching and buffering. The third topology, the CBA, is typically used in high-frequency applications where its low input impedance and wide bandwidth are advantageous [19,20].

Figure 1 provides a schematic overview of the three configurations: Figure 1a corresponds to the CEA, Figure 1b to the CCA, and Figure 1c to the CBA. In the CEA configuration, the BJT labeled Q_1 is biased by a voltage divider formed by resistors R_1 and R_2, which sets the dc base voltage and ensures the transistor operates in the active region. The collector and emitter are connected to resistors R_C and R_E, respectively, while R_L represents the external load resistance. A sinusoidal input voltage $v_i(t)$, applied in series with its internal resistance r_i, is capacitively coupled to the base terminal through capacitor C_1, which includes its equivalent series resistance (ESR) r_{C1}. The output voltage $v_o(t)$ is similarly extracted through capacitor C_2 (with ESR r_{C2}), which isolates the dc bias while allowing ac signal transfer to the load [19]. The dynamic behavior of the amplifier is captured by the collector, base, and emitter currents—$i_C(t)$, $i_B(t)$, and $i_E(t)$—as well as the load current $i_L(t)$ and output voltage $v_o(t)$.

Figures 1b and 1c illustrate the CCA and CBA configurations, respectively. Structurally, these topologies retain key elements from the CEA, including the voltage divider bias network (R_1 and R_2) and coupling capacitors (C_1 and C_2 with ESRs). The input source remains $v_i(t)$ in series with r_i, and $v_o(t)$ continues to represent the principal output variable. Each topology integrates a load resistor R_L, and the BJT labeled Q_1 remains the active element across all cases, maintaining design consistency for comparative analysis.
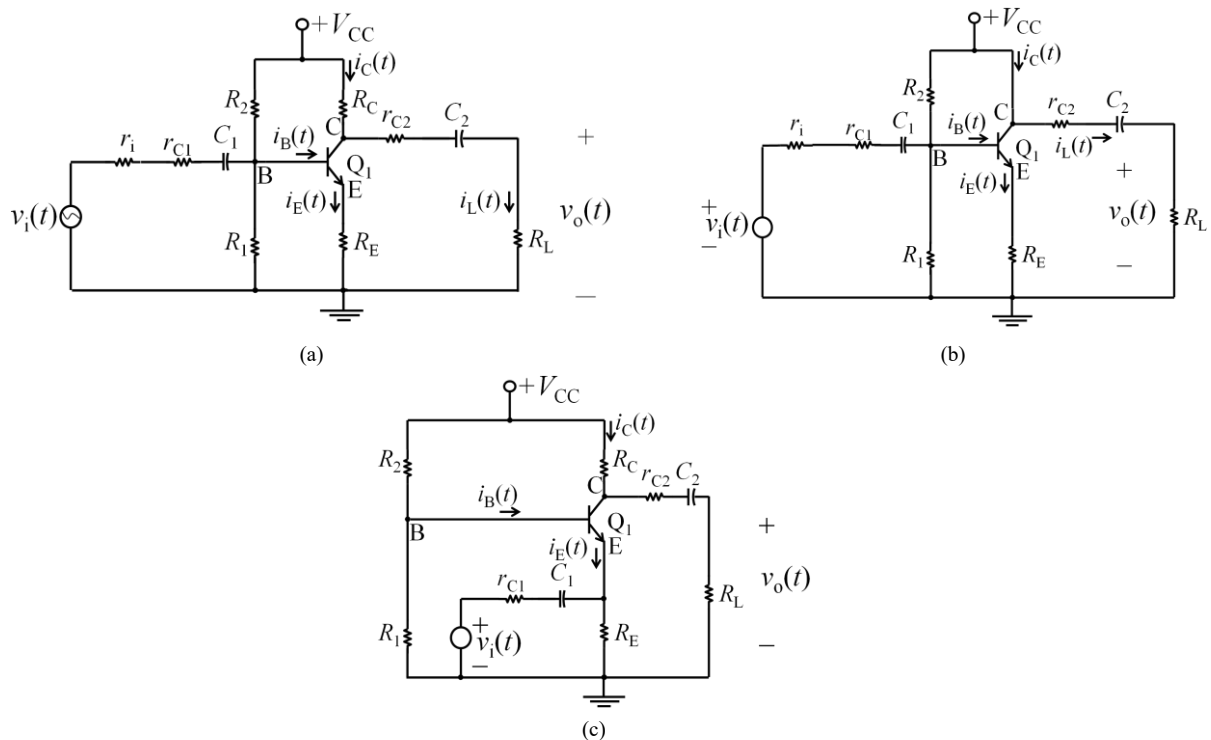

Figure 1. Various topologies of BJT-Amps are shown. (a) CEA. (b) CCA. (c) CBA.

3. Modeling of the common-emitter, common-collector, and common-base amplifiers

This section deals with the derivation of the fundamental equations governing the CEA, CCA, and CBA. The analysis includes considerations for both dc and ac operating conditions. To further refine the modeling approach, BJT-Amp are characterized under low-frequency and high-frequency models within the ac mode. Throughout this modeling process, transistor Q_1 is assumed to operate in the linear region, ensuring fidelity of signal amplification with due care to accuracy

and precision [19,20]. This fundamental approach sets the stage for a comprehensive understanding of the dynamic behavior exhibited by each amplifier configuration across a spectrum of operating conditions.

3.1. DC operation for CEA

It is notable that the equations derived for the CEA extend their validity to the CCA and CBA [19–21]. During dc operation, the coupling capacitors (C_1 and C_2) exhibit open-circuit behavior, resulting in a modified circuit configuration shown in Figure 2a, which is recognized as a dc-biased CEA [19,20]. In this scenario, V_{BE} refers to the dc voltage measured between the base and emitter terminals.

To simplify the analysis, the combination of resistors R_1, R_2, and the voltage source V_{CC} yields a Thevenin equivalent circuit, resulting in a specialized CEA circuit specifically designed for dc operation, as shown in Figure 2b.
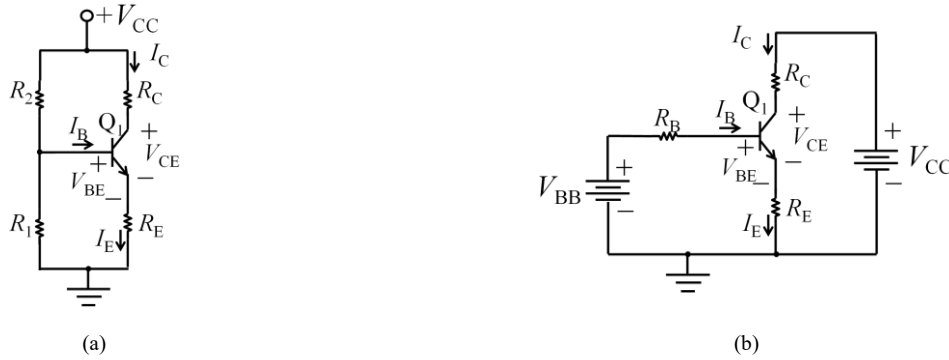

(a)   (b)

Figure 2. ECA operating in dc regime. (a) Topology in dc bias. The capacitors C_1 and C_2 act as open circuits. (b) Topology in dc bias with equivalent Thévenin input network.

Note that lowercase letters in Figure 2 are replaced with uppercase letters to indicate the representation of dc-only components. Key definitions in this context include:

$$V_{BB} = \frac{R_B}{R_2} \cdot V_{CC} \tag{1}$$

$$R_B = R_1 \| R_2 \tag{2}$$

Considering (1) and (2), the information shown in Figure 2b, and references [19,20], the operating point of the CEA can be precisely determined to achieve the maximum voltage output excursion, $v_o(t)$. This operating point is defined as follows:

$$V_{CE_Q} = \frac{1}{2} \cdot V_{CC} \tag{3}$$

$$I_{CE_Q} = \frac{V_{BB} - V_{BE}}{R_B / \beta + R_E} \tag{4}$$

Equation (4) explicitly denotes β as the gain in dc [19]. Since the underlying assumption is that Q_1 operates in the linear region, the expressions $I_{CQ} = \beta \cdot I_B$, $I_{EQ} \approx I_{CQ}$, and $V_{BE} = 0.7$ V can be confirmed. This thorough analysis provides a comprehensive understanding of the operating dynamics of the CEA under dc conditions and confirms the reliability of the established equations and circuit configurations.

3.2. AC operation for CEA in low frequency

The BJT amplifier contains strategically designed capacitors to couple the output to the load and to couple the voltage source to the base of the CEA. Although these capacitors are designed to remain open under dc conditions, they gradually deviate from the shorted state as the frequency decreases. As a result, their short-circuit capability degrades and they are not short-circuited anymore, so their behavior must be taken into account [22].

Figure 3a shows the small-signal model of CEA valid for low-frequency operation. If $\beta \gg 1$ and recognizing that $R_i = r_i + r_{C1}$ and $R_e' = \beta \cdot (hib + R_e)$, where $hib = hie/\beta$, a simplified version of the model in Figure 3a can be developed, which is described in Figure 3b. Finally, the model in Figure 3b can be further simplified by recognizing that the current-controlled current source and the resistor R_c can be combined in such a way as to produce a current-controlled voltage source connected in series with R_c. It is then easy to see that $R_o = R_c + r_{C2}$. This new version is shown in Figure 3c. The derivation of a state-space model from the representation in Figure 3c involves the identification of state variables (SVs), input and output. In this case, two state variables are identified, $v_{C1}(t)$ and $v_{C2}(t)$, with $v_i(t)$ as the input and $v_o(t)$ as the output. Kirchhoff's voltage (KVL) and current (KCL) laws are applied to the circuit in Figure 3c to formulate the state-space model, as shown:

$$\begin{cases} \dot{\mathbf{x}}(t) = \mathbf{A} \cdot \mathbf{x}(t) + \mathbf{B} \cdot u(t) \\ y(t) = \mathbf{C} \cdot \mathbf{x}(t) + D \cdot u(t) \end{cases} \tag{5}$$

Here, $\mathbf{x}(t)$ denotes the vector of state variables, $\mathbf{x}(t) = [v_{C1}(t), v_{C2}(t)]^T$. The variables $u(t)$ and $y(t)$ represent $v_i(t)$ and $v_o(t)$, respectively. Symbolically, $\mathbf{x}(t) \in \{\mathbb{R}\}^2$ and $\{u(t), y(t)\} \in \{\mathbb{R}\}$. The matrices $\mathbf{A}$, $\mathbf{B}$, and $\mathbf{C}$ denote the state, input, and output matrices, respectively while D denotes the direct-transmission constant. Their definitions are shown as follows:

$$\mathbf{A} = \begin{bmatrix} -\dfrac{1}{\tau_1} & 0 \\ -\dfrac{k_{21}}{\tau_2} & -\dfrac{1}{\tau_2} \end{bmatrix}, \mathbf{B} = \begin{bmatrix} \dfrac{1}{\tau_1} \\ \dfrac{k_{21}}{\tau_2} \end{bmatrix}, \mathbf{C} = \begin{bmatrix} -k_{32} \\ -k_{33} \end{bmatrix}^T, D = k_{31} \tag{6}$$

Symbolically, $\mathbf{A} \in \mathcal{M}_{2\times2} \{\mathbb{R}\}$, $\mathbf{B} \in \mathcal{M}_{2\times1} \{\mathbb{R}\}$, $\mathbf{C} \in \mathcal{M}_{1\times2} \{\mathbb{R}\}$, and $D \in \{\mathbb{R}\}$. Additionally, the constants τ_i ($i \in \{1, 2\}$) and k_{ji} ($j \in \{2, 3\}$) are given by:

$$\begin{cases} \tau_1 = C_1 \cdot (R_i + R_b \| R_{e'}) \\ \tau_2 = C_2 \cdot R_{L'} \end{cases}, \begin{cases} k_{21} = \dfrac{\beta \cdot R_e \cdot R_i \| R_b \| R_{e'}}{R_{e'} \cdot R_i} \\ k_{31} = \dfrac{\beta \cdot R_L \| R_o \cdot R_e \cdot R_i \| R_b \| R_{e'}}{R_o \cdot R_i \cdot R_{e'}} \\ k_{32} = \dfrac{k_{31}}{\beta} \\ k_{33} = \dfrac{R_L \| R_o}{R_o} \end{cases} \tag{7}$$

Also, from here, $R_{L'} = R_o + R_L$. Basically, τ_i and k_{ji} are the time constants related to the RC structures of the input and output of the small-signal model and the steady-state gains of the circuit, respectively. This meticulous formulation lays the groundwork for a comprehensive understanding of the CEAs' ac operation at low frequencies.

3.3. AC operation for CEA in high frequency

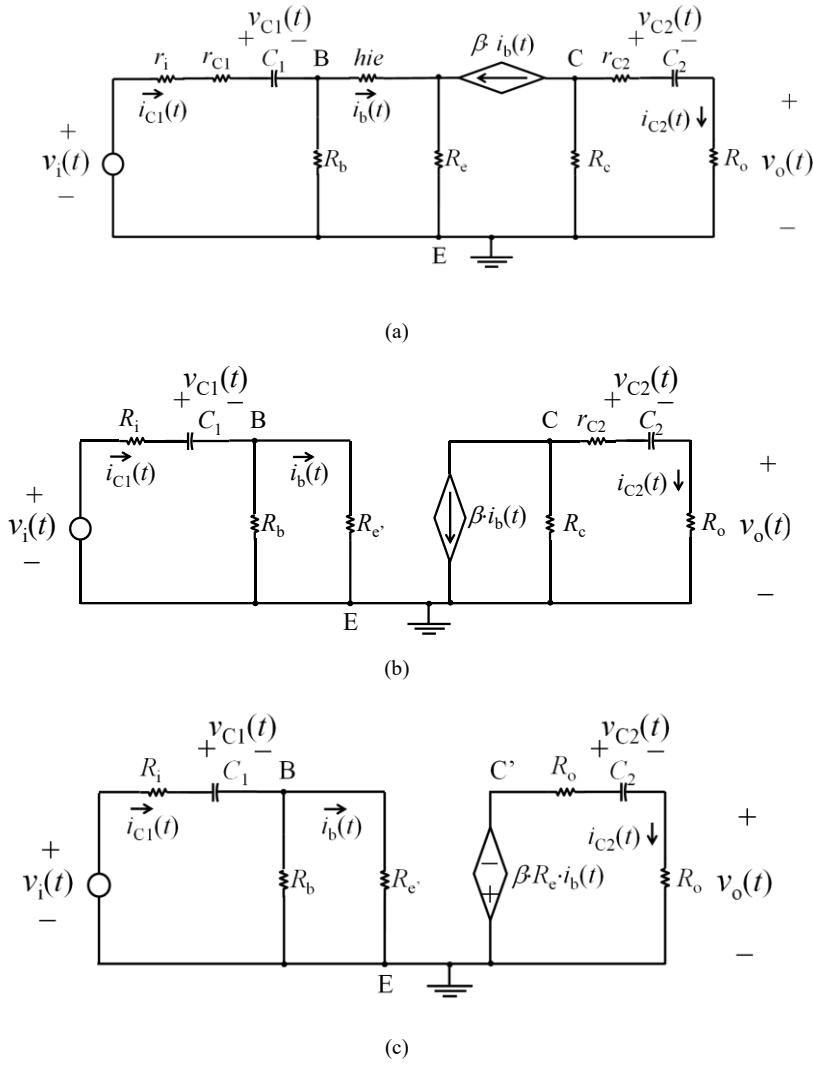To evaluate the high-frequency response of BJT-Amps, the π-hybrid model, which reflects the hybrid parameter model

Figure 3. Equivalent small-signal model, based on hybrid parameters for the CEA valid for low frequencies. (a) Non-simplified circuit of the small-signal model. (b) Simplified circuit considering $\beta \gg 1$, $R_i = r_i + r_{C1}$ and $R_{e'} = \beta \cdot (hib + R_e)$. (c) Simplified circuit considering the conversion of the controlled current source by a controlled voltage source.

discussed in subsection B [19,21], is essential. The high-frequency model for the CEA, shown in Figure 4a, uses the π-hybrid model. After identifying that $R_o = R_c \| R_L$ and considering that $r_{ce} \gg R_o$, it is possible to simplify the model eliminating $r_{b'c}$, which is much larger than all the other resistors in the circuit. Additionally, $r_{bb'}$ can be eliminated from the model since $r_{bb'} \ll r_{b'e}$. It should be noted that the input and base diffusion resistances are denoted by $r_{b'e}$ and $r_{bb'}$ respectively [22]. Finally, Miller's theorem [23] can be applied, where $C_M = C_{b'c} \cdot (1 - A_v)$ is the Miller capacitance, resulting in the equivalent circuit shown in Figure 4b. Also, $C_{b'c}$ is the collector junction capacitance. In practice, this capacitance is negligibly small at high frequencies [19,20]. The constant $g_m = 1/hib$. The model shown in Figure 4b can be simplified again by considering that $r_{ce} \gg R_o$, and that the impedance associated with the effective capacitance $C_{b'c} \cdot (1 - 1/A_v) \gg R_o$. Additionally, given that $R_{b'e} = R_b \| r_{b'e}$ and $C_t = C_{b'e} + C_M$, the simplified equivalent model is shown in Figure 4c. Finally, A_v represents the CEA gain for mid frequencies, which is defined as $A_v = -g_m \cdot R_o$ [19,20].

It is important to note that the B' terminal is the base junction, while B is the base terminal. The model assumes that the coupling capacitors (C_1 and C_2) act as short circuits. In addition, the equivalent series resistances, namely r_{C1} and r_{C2},
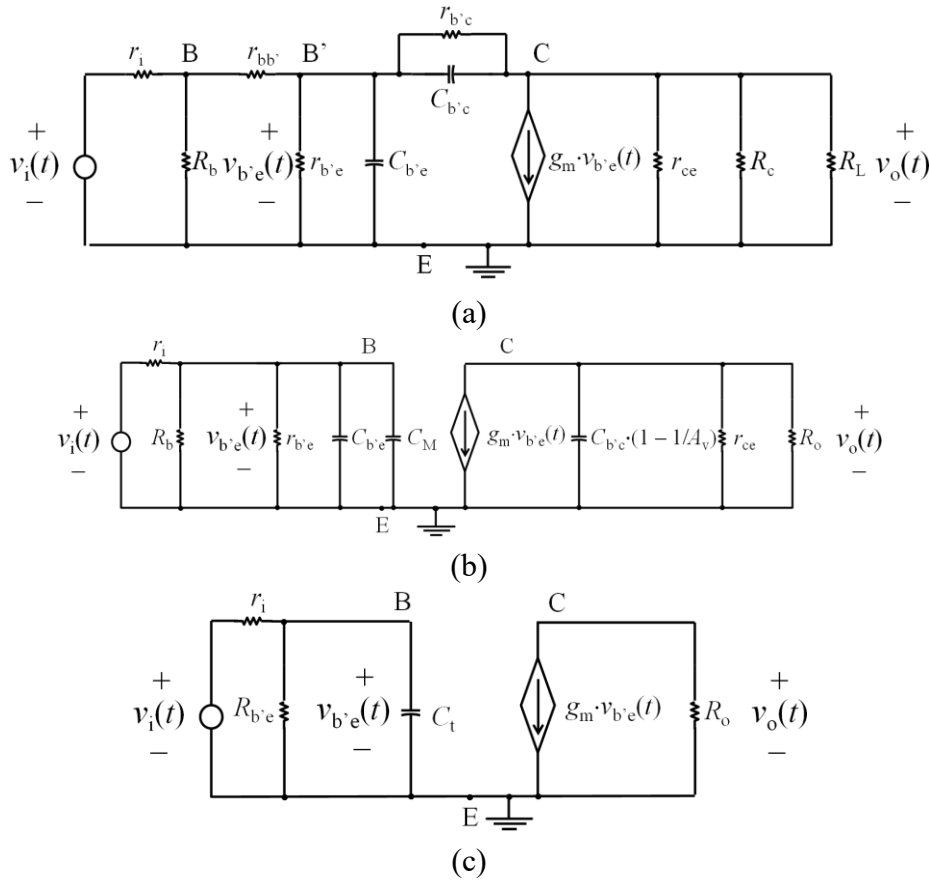
Figure 4. Equivalent small-signal model, based on π-hybrid parameters for the CEA valid for high frequencies. (a) Non-simplified circuit of the small-signal model. (b) Simplified circuit considering $r_{ce} \gg R_o$, also $r_{b'c}$ is much larger than all the resistors and resistors in the circuit. $r_{bb'} \ll r_{b'e}$ is considered as well, and finally the Miller theorem is applied where $C_M = C_{b'c}\cdot(1 - A_v)$. (c) Simplified circuit considering that $r_{ce} \gg R_o$ and $C_{b'c}\cdot(1 - 1/A_v) \gg R_o$.

are omitted from the model due to the high-frequency nature of the analysis [24].

The capacitance $C_{b'e}$ combines the emitter diffusion capacitance and the junction capacitance. Due to the significant difference in magnitude between these capacitances, $C_{b'e}$ approximates the diffusion capacitance, also known as the base load capacitance [19,20].

Incorporating the definition of A_v into the definition of C_M, the new definition of Miller capacitance can be stated as:

$$C_M = C_{b'c}\cdot\left(1 + g_m\cdot R_o\right) \tag{8}$$

Like the low-frequency analysis, it is imperative to identify the SVs, input, and output before deriving the dynamic equations. This high-frequency model has a singular state variable $v_{b'e}(t)$, with $v_i(t)$ as input and $v_o(t)$ as output. Denoted $x(t) = v_{b'e}(t)$, $u(t) = v_i(t)$, and $y(t) = v_o(t)$, considering that $\{x(t), u(t), y(t)\} \in \{\mathbb{R}\}$, and performed KVL and KCL to model in Figure 4c, the high-frequency dynamic model for the CEA is expressed as:

$$\begin{cases} \dfrac{dx(t)}{dt} = \dfrac{k_{11}}{\tau_1}\cdot u(t) - \dfrac{1}{\tau_1}\cdot x(t) \\ \quad y(t) = -R_o\cdot g_m\cdot x(t) \end{cases} \tag{9}$$

where $\tau_1 = C_t\cdot R_{b'e}\|r_i$, and $k_{11} = (R_{b'e}\|r_i)/r_i$. This comprehensive dynamic model provides detailed insights into the high-frequency behavior of the CEA.

3.4. AC operation for CCA in low frequency

The dynamic characteristics of the CCA in the low-frequency operating range are similar to those of the CEA [19–21]. The valid low-frequency small-signal model based on the hybrid parameters of the CCA is illustrated in Figure 5a. In this case, R_i can be simplified as the sum of r_i and r_{C1}, as shown in Figure 5b.

In this model, two SVs are identified, labeled $v_{C1}(t)$ and $v_{C2}(t)$, with the input and output labeled $v_i(t)$ and $v_o(t)$, respectively. Applying KVL and KVC to the circuit in Figure 5b yields a state-space model in the form of (5), where the state matrix **A**, input matrix **B**, output matrix **C**, and constant D are defined as follows:

$$\mathbf{A} = \begin{bmatrix} -\dfrac{1}{\tau_1} & -\dfrac{k_{11}}{\tau_1} \\ -\dfrac{k_{21}}{\tau_2} & -\dfrac{1}{\tau_2} \end{bmatrix}, \mathbf{B} = \begin{bmatrix} \dfrac{k_{12}}{\tau_1} \\ \dfrac{k_{21}}{\tau_2} \end{bmatrix}, \mathbf{C} = \begin{bmatrix} -k_{31} \\ -k_{32} \end{bmatrix}^{\mathrm{T}}, D = k_{31} \tag{10}$$

Furthermore, $\mathbf{x}(t) = [v_{C1}(t), v_{C2}(t)]^{\mathrm{T}}$, $u(t) = v_i(t)$, and $y(t) = v_o(t)$, symbolizing the SV vector, input, and output, respectively. Symbolically, $\mathbf{A} \in \mathcal{M}_{2x2} \in \{\mathbb{R}\}$, $\mathbf{B} \in \mathcal{M}_{2x1} \{\mathbb{R}\}$, $\mathbf{C} \in \mathcal{M}_{1x2} \{\mathbb{R}\}$, and $D \in \{\mathbb{R}\}$. In addition, $\mathbf{x}(t) \in \{\mathbb{R}^2\}$ and $\{u(t), y(t)\} \in \{\mathbb{R}\}$. The constants τs and ks are given by (11). From here, R_{eqx} ($x \in \{1, 2, 3, 4, 5\}$) are defined in (12).

3.5. AC operation for CCA in high frequency

The CCA is characterized by a voltage gain close to one, making it a common choice for handling high frequencies. Its topology, based on the small-signal π-hybrid parameter model, is shown in Figure 5 6a. Additionally, it is important to note that these amplifiers have a capacitive load, which is why a C_L capacitor is included with its corresponding ESR, with an appropriate value that does not allow the C_L to be turned into a short circuit [19,20]. Figure 6a can be simplified by (12) converting the voltage sources, the non-controlled and the controlled, by their dual current sources, and by considering $R_i = r_i \| R_b$, as shown in Figure 6b. The circuit can be further simplified by converting the non-controlled current source into
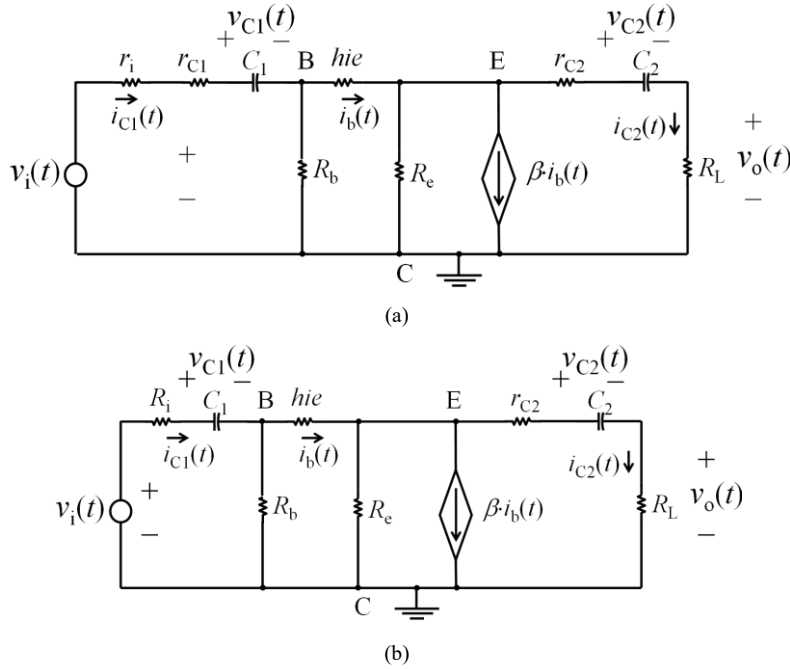

(a)

(b)

Figure 5. Equivalent small-signal model, based on hybrid parameters for the CCA valid for low frequencies. (a) Non-simplified circuit of the small-signal model. (b) Simplified circuit considering $R_i = r_i + r_{C1}$.

$$\begin{cases} \tau_1 = C_1 \cdot R_{\text{eq}_2} \\ \tau_2 = C_2 \cdot \left(\dfrac{R_{\text{eq}_5}}{R_\text{b} \cdot R_\text{i} + R_\text{b} \cdot hie + R_{\text{eq}_1} + \beta \cdot R_\text{e} \cdot R_\text{i}} \right) \end{cases}$$

$$\begin{cases} k_{11} = \dfrac{R_\text{b} \cdot R_\text{e} \cdot R_{\text{eq}_2}}{R_{\text{eq}_5}} \\ k_{12} = R_{\text{eq}_2}{}^2 \\ k_{21} = \dfrac{R_{\text{eq}_1}}{R_\text{b} \cdot R_\text{i} + (R_\text{b} + R_\text{i}) \cdot hie + R_{\text{eq}_1} + \beta \cdot R_\text{e} \cdot R_\text{i}} \\ k_{31} = \dfrac{R_\text{L} \cdot R_{\text{eq}_1}}{R_{\text{eq}_5}} \\ k_{32} = \left(\dfrac{R_\text{b} \cdot R_\text{c} + (R_\text{b} + R_\text{i}) \cdot hie + R_{\text{eq}_1} + \beta \cdot R_\text{e} \cdot R_\text{i}}{R_{\text{eq}_5}} \right) \cdot R_\text{L} \end{cases} \tag{11}$$

$$\begin{cases} R_{\text{eq}_1} = \beta \cdot R_\text{b} \cdot R_\text{e} \\ R_{\text{eq}_2} = \dfrac{(R_\text{L} + R_\text{e}) \cdot R_\text{b} + (R_\text{L} + R_\text{e} + r_{\text{C}_2}) \cdot hie}{R_{\text{eq}_5}} + \dfrac{r_{\text{C}_2} \cdot R_\text{b} + (R_\text{L} + r_{\text{C}_2}) \cdot \beta \cdot R_\text{e}}{R_{\text{eq}_5}} \\ R_{\text{eq}_3} = \dfrac{R_{\text{eq}_1}}{R_{\text{eq}_5}} \\ R_{\text{eq}_4} = \dfrac{R_\text{b} \cdot (R_\text{L} + R_\text{e} + r_{\text{C}_2})}{R_{\text{eq}_5}} \\ R_{\text{eq}_5} = (R_\text{b} + R_\text{i}) \cdot (R_\text{L} + R_\text{e} + r_{\text{C}_2}) \cdot (R_\text{i} \| R_\text{b} + hie) + R_{\text{eq}_1} \cdot (R_\text{L} + r_{\text{C}_2}) + \beta \cdot R_\text{e} \cdot R_\text{i} \cdot (R_\text{i} + r_{\text{C}_2}) \end{cases} \tag{12}$$

its voltage dual, as shown in Figure 6c. Also, this model represents a modified equivalent circuit in which the Miller capacitance (C_M) is absent due to the proximity of the voltage gain to unity [19].

Upon analyzing the model presented in Figure 6c, it becomes apparent that the system consists of two SVs, namely $v_{\text{Cb'c}}(t)$ and $v_{\text{CL}}(t)$, with an identification of an input and an output, namely $v_\text{i}(t)$ and $v_\text{o}(t)$, respectively. Therefore, the following definitions can be made $\mathbf{x}(t) = [v_{\text{Cb'c}}(t), v_{\text{CL}}(t)]^\text{T}$, $u(t) = v_\text{i}(t)$, and $y(t) = v_\text{o}(t)$. These correspond to the state vector, input, and output, respectively, all of which are scalars. By applying KVL and KCL to the model in Figure 6c, the dynamical equations and the output equation can be derived and represented as the state-space model defined in (5). In this case the state matrix ($\mathbf{A}$), the input matrix ($\mathbf{B}$), the output matrix ($\mathbf{C}$), and the direct-transmission constant (D) are defined as follows:

$$\mathbf{A} = \begin{bmatrix} -\dfrac{1}{\tau_1} & 0 \\ -\dfrac{k_{22}}{\tau_2} & -\dfrac{1}{\tau_2} \end{bmatrix}, \mathbf{B} = \begin{bmatrix} \dfrac{k_{11}}{\tau_1} \\ \dfrac{k_{21}}{\tau_2} \end{bmatrix}, \mathbf{C} = \begin{bmatrix} -k_{31} \\ 1 \end{bmatrix}^\text{T}, D = k_{32} \tag{13}$$

On the other hand, $\mathbf{A} \in \mathcal{M}_{2\text{x}2}\{\mathbb{R}\}$, $\mathbf{B} \in \mathcal{M}_{2\text{x}1}\{\mathbb{R}\}$, $\mathbf{C} \in \mathcal{M}_{1\text{x}2}\{\mathbb{R}\}$, and $D \in \{\mathbb{R}\}$. The constants of the model are given by:

$$\begin{cases} \tau_1 = C_{\text{b'e}} \cdot R_\text{i} \\ \tau_2 = C_\text{L} \cdot (R_\text{L} + r_{\text{C}_\text{L}}) \end{cases}, \begin{cases} k_{11} = \dfrac{R_\text{i}}{r_\text{i}} \\ k_{21} = \beta \cdot \dfrac{R_\text{L}}{r_\text{i}} \end{cases}, \begin{cases} k_{22} = \beta \cdot \dfrac{R_\text{L}}{R_\text{i}} \\ k_{31} = \beta \cdot \dfrac{R_\text{L} \| r_{\text{C}_\text{L}}}{R_\text{i}} \\ k_{32} = \beta \cdot \dfrac{R_\text{L} \| r_{\text{C}_\text{L}}}{r_\text{i}} \end{cases} \tag{14}$$
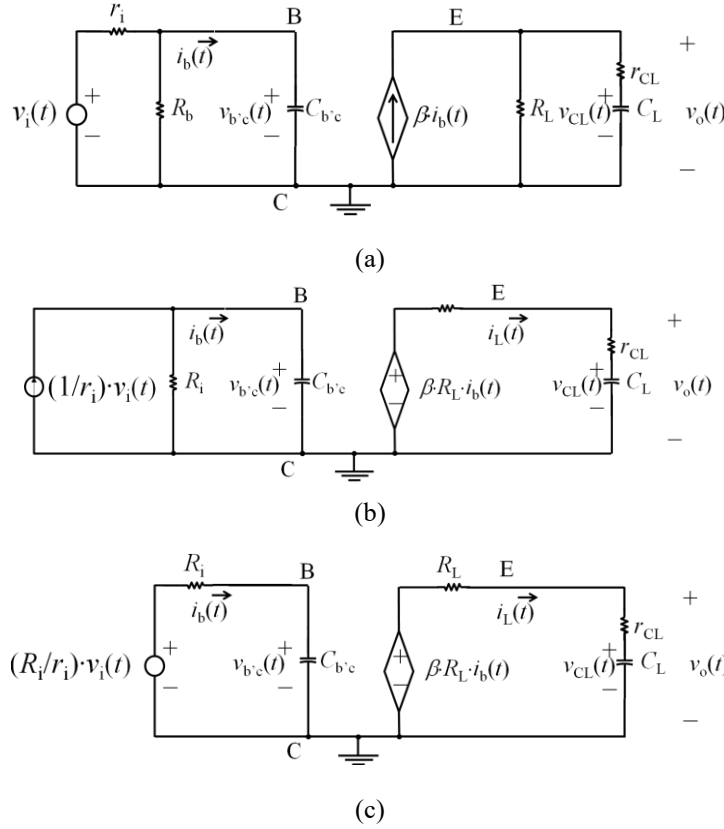
(a)

(b)

(c)

Figure 6. Equivalent small-signal model, based on π-hybrid parameters for the CCA valid for high frequencies. (a) Non-simplified circuit of the small-signal model. (b) Simplified circuit considering converting non- controlled and controlled voltages into their dual-current sources and taking into account $R_i = r_i \| R_b$. (c) Simplified circuit considering that $r_{ce} \gg R_o$ and $C_{b'c} \cdot (1 - 1/A_v) \gg R_o$.

Symbolically, $\mathbf{x}(t) \in \{R\}^2$ and $\{u(t), y(t)\} \in \{R\}$.

3.6. AC operation for CBA in low frequency

It is worth noting that this topology does not produce any current gain, but it does produce voltage gain [20]. Figure 7a illustrates the small-signal model based on hybrid parameters, which is valid for low frequencies of the CBA. Upon observing the model in Figure 7a, it can be determined that $R_i = r_i + r_{C1} + hib$ and that the output admittance is very small, indicating that $1/hob \rightarrow \infty$ and can be neglected. Therefore, the simplified model in Figure 7b is presented.

This model has two SVs, $v_{C1}(t)$ and $v_{C2}(t)$, an input labeled $v_i(t)$, and an output labeled $v_o(t)$. The state vector $\mathbf{x}(t)$, input $u(t)$, and output $y(t)$ can be defined as $\mathbf{x}(t) = [v_{C1}(t), v_{C2}(t)]^T$, $u(t) = v_i(t)$, and $y(t) = v_o(t)$, respectively. Symbolically, $\mathbf{x}(t) \in \{\mathbb{R}^2\}$, and $\{u(t), y(t)\}$ is in $\{\mathbb{R}\}$. Applying the KVL and KCL to the model in Figure 7b, the state-space model is derived and described in (5). The state matrix $\mathbf{A}$, input matrix $\mathbf{B}$, output matrix, and direct-transmission constant D are defined as follows:

$$\mathbf{A} = \begin{bmatrix} -\dfrac{1}{\tau_1} & 0 \\ -\dfrac{k_{21}}{\tau_2} & 0 \end{bmatrix}, \mathbf{B} = \begin{bmatrix} \dfrac{1}{\tau_1} \\ \dfrac{k_{21}}{\tau_2} \end{bmatrix}, \mathbf{C} = \begin{bmatrix} -k_{31} \\ 1 \end{bmatrix}^T, D = k_{31} \tag{15}$$

Symbolically, $\mathbf{A} \in \mathcal{M}_{2x2} \in \{\mathbb{R}\}$, $\mathbf{B} \in \mathcal{M}_{2x1} \{\mathbb{R}\}$, $\mathbf{C} \in \mathcal{M}_{1x2} \{\mathbb{R}\}$, and $D \in \{\mathbb{R}\}$. The constants τ_i $(i \in \{1, 2\})$ and k_{j1}
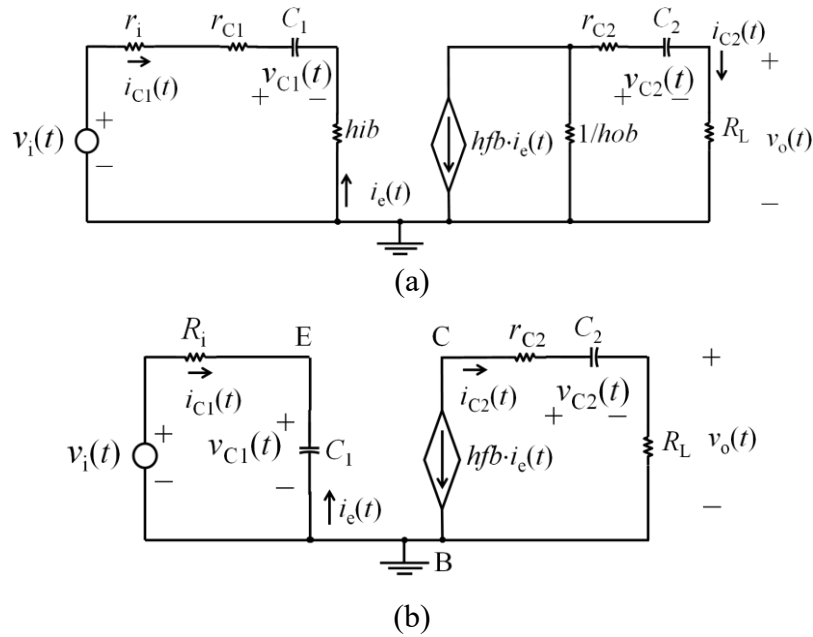
(a)

(b)

Figure 7. Equivalent small-signal model, based on hybrid parameters for the CBA valid for low frequencies. (a) Non-simplified circuit of the small-signal model. (b) Simplified circuit considering that $1/hob \rightarrow \infty$ and $R_i = r_i + r_{C1} + hib$.

($j \in \{2, 3\}$) incorporated in (15) are defined as follows:

$$\begin{cases} \tau_1 = C_1 \cdot R_i \\ \tau_2 = C_2 \cdot R_i \end{cases}, \begin{cases} k_{21} = hfb \\ k_{31} = \dfrac{hfb}{R_i} \end{cases} \tag{16}$$

3.7. AC operation for CBA in high frequency

According to [19], the CBA has a superior high-frequency response compared to the CEA. This attribute can often result in a higher voltage gain, which in turn causes the Miller capacitance to become significantly more substantial. As shown in Figure 8, the Miller effect in the circuit has less impact at high frequencies. This is due to the small-signal model based on π-hybrid parameters.

The model includes two SVs, $v_{b'e}(t)$ and $v_o(t)$, denoted as $x_1(t)$ and $x_2(t)$, respectively. Therefore, $\mathbf{x}(t) = [x_1(t), x_2(t)]^T$ is the state vector. On the other hand, the input ($u(t)$) and output ($y(t)$) are identified as $v_i(t)$ and $v_o(t)$, respectively. Symbolically, $\mathbf{x}(t) \in \{\mathbb{R}^2\}$ and $\{u(t), y(t)\} \in \{\mathbb{R}\}$. The state-space model defined in (5) remains consistent, with the state matrix ($\mathbf{A}$), input matrix ($\mathbf{B}$), output matrix ($\mathbf{C}$), and direct-transmission constant (D) specified as follows:

$$\mathbf{A} = \begin{bmatrix} -\dfrac{1}{\tau_1} & 0 \\ \dfrac{k_{21}}{\tau_2} & -\dfrac{1}{\tau_2} \end{bmatrix}, \mathbf{B} = \begin{bmatrix} \dfrac{k_{11}}{\tau_1} \\ 0 \end{bmatrix}, \mathbf{C} = \begin{bmatrix} 0 \\ 1 \end{bmatrix}^T, D = 0 \tag{17}$$

where symbolically, $\mathbf{A} \in \mathcal{M}_{2x2} \in \{\mathbb{R}\}$, $\mathbf{B} \in \mathcal{M}_{2x1} \{\mathbb{R}\}$, $\mathbf{C} \in \mathcal{M}_{1x2} \{\mathbb{R}\}$, and $D \in \{\mathbb{R}\}$. Also, the τ- and k-constants are given by (18).

Table 1 summarizes the small-signal models for BJT-Amps configured as CEA, CCA, and CBA, with their corresponding mathematical models at low and high frequencies.
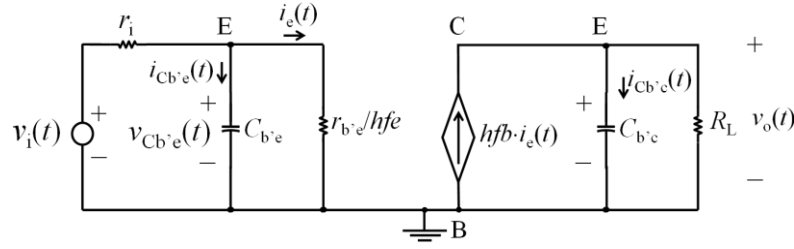
Figure 8. Equivalent small-signal model, based on π-hybrid parameters for the CBA valid for high frequencies.

$$\begin{cases} \tau_1 = C_{b'e} \cdot r_i \| \left(\dfrac{r_{b'e}}{hfe}\right) \\ \tau_2 = C_L \cdot R_L \end{cases} , \quad \begin{cases} k_{11} = \dfrac{r_i \| \left(\dfrac{r_{b'e}}{hfe}\right)}{r_i} \\ k_{21} = \dfrac{hfb \cdot R_L}{\dfrac{r_{b'e}}{hfe}} \end{cases} \tag{18}$$

4. Solution of the dynamic and state equations of BJT-amps

In this section, the time expressions of each of the dynamic and state variables related to the models of BJT amplifiers valid in the low and high frequency ranges, derived in the previous section, are obtained. This study makes it possible to obtain a more complete knowledge of the parameters involved in the dynamics of these amplifiers, including both their dynamic and state variables and their selected output variables. With this knowledge, better design conditions can be established.

As can be seen below, most BJT amplifier models are represented by their state space models. In most cases in this study, the system consists of a state vector and a scalar input and output. It is well known that the state space model consists of a state equation and an output equation [25–27]. Therefore, it is necessary to solve the state equation, since in most cases the output variable is composed of its SVs, and then, knowing the expressions that model the dynamics of the SVs, the dynamics of the output variable [25–27] will also be known.

In most of the low and high frequency BJT amplifier models studied in this paper, the state equation is defined as follows:

$$\frac{d\mathbf{x}(t)}{dt} = \mathbf{A} \cdot \mathbf{x}(t) + \mathbf{B} \cdot u(t) \Rightarrow \frac{d\mathbf{x}(t)}{dt} - \mathbf{A} \cdot \mathbf{x}(t) = \mathbf{B} \cdot u(t) \tag{19}$$

From (19) where, as already mentioned, the variables $\mathbf{x}(t)$ and $u(t)$ are the state vector and input variable, respectively, and the matrices $\mathbf{A}$ and $\mathbf{B}$ are the state and output matrices, respectively. Furthermore, (19) is a first-order linear differential equation. It can be solved by many methods, such as using integration factors, linear differential operators, and using the Laplace variable [26,27], among others. However, taking advantage of (19) being in its state equation form, it is solved using the state transition matrix ($\boldsymbol{\Phi}(t)$) [26–28]. Note that all initial conditions of the states of each of the models are zero, i.e. $\mathbf{x_0} = \mathbf{0}$, where $\mathbf{x_0}$ is the vector of initial state conditions. Symbolically, $\mathbf{x_0} \in \{\mathbb{R}^2\}$.

Defining $\boldsymbol{\Phi}(t) = e^{(\mathbf{A} \cdot t)}$ and multiplying it by $\boldsymbol{\Phi}(-t)$ on both sides of (19), it follows to (20). The mathematical structure described in (20) can be recognized as the result of applying a derivation using the chain rule (21). Therefore, integrating both sides of (20) from zero to t yields a new expression given by (22).

Table 1. Summary of the small-signal models for CEA, CCA, and CBA.

BJT-Amp	Small-signal model for low frequency	Small-signal model for high frequency	State-space model or dynamical equation — High frequency	State-space model or dynamical equation — Low frequency
CEA			$$\begin{cases} \dfrac{dx(t)}{dt} = \dfrac{1}{R_i \cdot (C_M + C_{b'e})} \cdot (K_i \cdot u(t) - x(t)) \\ y(t) = -R_o \cdot g_m \cdot x(t) \end{cases}$$	$$\begin{cases} \dot{\mathbf{x}}(t) = \mathbf{A} \cdot \mathbf{x}(t) + \mathbf{B} \cdot u(t) \\ y(t) = \mathbf{C} \cdot \mathbf{x}(t) + D \cdot u(t) \end{cases}$$
CCA			$$\begin{cases} \dfrac{dx(t)}{dt} = \dfrac{1}{C_{b'c} \cdot (R_i \cdot R_{bb'} - R_B^2)} \cdot (R_B \cdot u(t) - R_i \cdot x(t)) \\ y(t) = R_o \cdot g_m \cdot x(t) \end{cases}$$	$$\begin{cases} \dot{\mathbf{x}}(t) = \mathbf{A} \cdot \mathbf{x}(t) + \mathbf{B} \cdot u(t) \\ y(t) = \mathbf{C} \cdot \mathbf{x}(t) + D \cdot u(t) \end{cases}$$
CBA			$$\begin{cases} \dot{\mathbf{x}}(t) = \mathbf{A} \cdot \mathbf{x}(t) + \mathbf{B} \cdot u(t) \\ y(t) = \mathbf{C} \cdot \mathbf{x}(t) + D \cdot u(t) \end{cases}$$	$$\begin{cases} \dot{\mathbf{x}}(t) = \mathbf{A} \cdot \mathbf{x}(t) + \mathbf{B} \cdot u(t) \\ y(t) = \mathbf{C} \cdot \mathbf{x}(t) + D \cdot u(t) \end{cases}$$

$$e^{-\mathbf{A}\cdot t}\cdot\frac{d\mathbf{x}(t)}{dt} - \mathbf{A}\cdot e^{-\mathbf{A}\cdot t}\cdot\mathbf{x}(t) = e^{-\mathbf{A}\cdot t}\cdot\mathbf{B}\cdot u(t) \tag{20}$$

$$\frac{d}{dt}\left(e^{-\mathbf{A}\cdot t}\cdot\mathbf{x}(t)\right) = e^{-\mathbf{A}\cdot t}\cdot\mathbf{B}\cdot u(t) \tag{21}$$

$$e^{-\mathbf{A}\cdot t}\cdot\mathbf{x}(t) - \mathbf{x}_0 = \int_0^t e^{-\mathbf{A}\cdot\psi}\cdot\mathbf{B}\cdot u(\psi)\cdot d\psi \Rightarrow \mathbf{x}(t) = e^{-\mathbf{A}\cdot t}\cdot\mathbf{x}_0 + \int_0^t e^{-\mathbf{A}\cdot(t-\psi)}\cdot\mathbf{B}\cdot u(\psi)\cdot d\psi$$

$$\Rightarrow \mathbf{x}(t) = \mathbf{\Phi}(t)\cdot\mathbf{x}_0 + \int_0^t \mathbf{\Phi}(t-\psi)\cdot\mathbf{B}\cdot u(\psi)\cdot d\psi \tag{22}$$

Thus, (22) is the solution of (19). Equation (19) reveals that $\mathbf{x}(t)$ is the sum of two terms: one resulting from the initial state transition and the other from the input to the system. Therefore, $\mathbf{x}(t)$ describes the change in state relative to the initial conditions $\mathbf{x}_0$ and the input $u(t)$. In current state-space theory [26–28], (22) can be defined as:

$$\mathbf{x}(t) = \mathbf{x}_{zi}(t) + \mathbf{x}_{zs}(t) \tag{23}$$

$\mathbf{x}_{zi}(t)$ represents the zero-input response (i.e., $u(t) = 0$), and $\mathbf{x}_{zs}(t)$ represents the zero-state response (i.e., $\mathbf{x}_0 = \mathbf{0}$). Finally, and according to [26], $\mathbf{\Phi}(t)$ can be found and described as follows:

$$\mathbf{\Phi}(t) = e^{(\mathbf{A}\cdot t)} = \mathscr{L}^{-1}[(s\cdot\mathbf{I} - \mathbf{A})^{-1}] \tag{24}$$

Here, s is the Laplace operator, and $\mathbf{I}$ is the identity matrix of the same size as $\mathbf{A}$. With this information, it is possible to solve all the state equations associated with the dynamic models considered in this article. The process begins by obtaining $\mathbf{\Phi}(t)$ and then computing it in (22).

4.1. Solution of the CEA low frequency small signal model

The matrix $\mathbf{A}$ that corresponds to the CEA model is defined in (6). By computing (24), it is then possible to obtain the following:

$$\mathbf{\Phi}(t) = \begin{bmatrix} e^{-\frac{t}{\tau_1}} & 0 \\ c\cdot\left(e^{\frac{t}{\tau_1}} + e^{-\frac{t}{\tau_2}}\right) & e^{-\frac{t}{\tau_2}} \end{bmatrix}, \quad \mathbf{\Phi}(t-\psi) = \begin{bmatrix} e^{-\frac{t-\psi}{\tau_1}} & 0 \\ c\cdot\left(e^{-\frac{t-\psi}{\tau_1}} + e^{\frac{t-\psi}{\tau_2}}\right) & e^{\frac{t-\psi}{\tau_2}} \end{bmatrix} \tag{25}$$

From here, $c = k_{21}\cdot\tau_1/(\tau_1 - \tau_2)$. Also, k_{21}, τ_{one}, and τ_2 are defined in (7). After substituting (25) into (22) and performing some algebraic manipulations, the expressions of the SVs associated with this model are given by (26).

Equation (7) defines both k_{21} and τ_1 and τ_2. Also, $P_{i1} = 1/\tau_i$, $Q_{11} = P_{11}\cdot V$, $Q_{22} = k_{21}/(\tau_2\cdot\text{sqrt}(P_{11}^2 + \omega^2))$, and $Q_{23} = Q_{22}\cdot\sin(\theta)$. Finally, $j = \text{atan}(\omega/P_{i1})$ where $j \in \{\theta, \phi\}$ and $i \in \{1, 2\}$. Also, $\delta = \theta - \phi$ where V is the peak-to-peak voltage of the $v_i(t)$. Analyzing the dynamics of $v_{C1}(t)$ and $v_{C2}(t)$ and computing (5), the output expression is derived, which in this case is $v_o(t)$.

Expressions (26) describe the dynamic behavior of a system through its state variables, $v_{C1}(t)$ and $v_{C2}(t)$, as they evolve over time. These expressions reveal a complex interaction between oscillatory components and transient decay. The sinusoidal terms, modulated by exponential decay factors, confidently represent the system's response to external inputs and initial conditions. The magnitudes of these sinusoids are normalized by the square root of the sum of the squares of the

$$\begin{cases} v_{C_1}(t) = \dfrac{Q_{11}}{\sqrt{P_{11}{}^2 + \omega^2}} \cdot (\sin(\omega \cdot t - \theta) + \sin(\theta) \cdot e^{-P_{11} \cdot t}) \\[4mm] v_{C_2}(t) = \dfrac{Q_{21}}{\sqrt{P_{21}{}^2 + \omega^2}} \cdot (\sin(\omega \cdot t - \varphi) + \sin(\varphi) \cdot e^{-P_{21} \cdot t}) - \\[4mm] -\dfrac{Q_{22}}{\sqrt{P_{21}{}^2 + \omega^2}} \cdot (\sin(\omega \cdot t - \delta) + \sin(\delta) \cdot e^{-P_{21} \cdot t}) - \dfrac{Q_{23}}{\sqrt{P_{21}{}^2 + \omega^2}} \cdot (e^{-P_{11} \cdot t} - e^{-P_{21} \cdot t}) \end{cases} \qquad (26)$$

frequency and characteristic frequencies (P_{11} and P_{21}), which dictate the magnitude of oscillations. The coefficients Q_{11} and Q_{21} regulate the amplitudes of these sinusoids. The temporal order of these oscillations is determined by the phase shifts θ, ϕ, and δ. Additionally, the system's damping is controlled by exponential terms with decay rates P_{11} and P_{21}, with higher values indicating faster convergence to steady state. Overall, this system is characterized by a strong interaction between state variables. The terms in the equations account for the difference between characteristic frequencies of state variables, which affects their transient behavior and stability. These equations shed light on the dynamics, stability, and interactions between components of the system, providing a detailed understanding of its transient response.

4.2. Solution of the CEA high frequency small signal model

The CEA's high-frequency dynamic model is represented by a single equation of state, which is not solved through the use of $\mathbf{\Phi}(t)$. However, by making slight modifications to the state equation in (9), the state equation to be solved is defined as:

$$\frac{dv_{b'e}(t)}{dt} + P_{11} \cdot v_{b'e}(t) = Q_{11} \cdot \sin(\omega \cdot t) \qquad (27)$$

where $P_{11} = 1/\tau_1$ and $Q_{11} = k_{11} \cdot V/\tau_1$. The values of τ_1 and k_{11} are defined in subsection C titled 'ac operation for CEA in high frequency.

Equation (27) is a first-order linear differential equation that can be solved by using an integration factor (*IF*) to convert it into an exact equation. In this case, $IF = e^{-P11 \cdot t}$. By multiplying both sides of (27) with *IF*, the following form of this equation can be identified:

$$\frac{d}{dt}\left(e^{-P_{11} \cdot t} \cdot v_{b'e}(t)\right) = Q_{11} \cdot e^{-P_{11} \cdot t} \cdot \sin(\omega \cdot t) \qquad (28)$$

Integrating both sides of (28) and considering zero initial conditions, the time expression of $v_{b'e}(t)$ is obtained and expressed as:

$$v_{b'e}(t) = \frac{Q_{11}}{\sqrt{P_{11}{}^2 + \omega^2}} \cdot \left(\sin\left(\omega \cdot t - \theta\right) + \sin\left(\theta\right) \cdot e^{-P_{11} \cdot t}\right) \qquad (29)$$

where $\theta = \operatorname{atan}(\omega/P_{11})$. Finally, replacing (29). Finally, by replacing (29) which has already been evaluated in (9), the voltage $v_o(t)$ is obtained.

Equation (29) demonstrates the time-dependent behavior of $v_{b'e}(t)$, exhibiting both oscillatory and decaying characteristics. The amplitude of the sinusoidal component is determined by the coefficient Q_{11} and the ratio of the

frequency to the square root of the sum of the squares of the characteristic frequency (P_{11}) and the frequency. This ratio controls the magnitude of the oscillation, with higher frequencies or lower fundamental frequencies resulting in larger amplitudes. The phase shift θ determines the temporal orientation of the sinusoidal waveform, affecting its position on the time axis. The exponential term with decay rate P_{11} regulates the damping of the oscillation, with higher values resulting in faster decay. This equation offers insight into the evolution of $v_{b'e}(t)$ over time, capturing both its oscillatory behavior and its tendency to converge to a steady-state value determined by the decay term.

4.3. Solution of the CCA low frequency small signal model

To obtain the $\mathbf{\Phi}(t)$ matrix, (24) is calculated using the matrix $\mathbf{A}$ related to the low frequency CCA defined in (10). The computation of (24) results in the expressions given by:

$$\mathbf{\Phi}(t) = \begin{bmatrix} c_{11} \cdot e^{-\gamma \cdot t} + c_{11}^* \cdot e^{-\gamma^* \cdot t} & -c_{12} \cdot \left(e^{-\gamma \cdot t} - e^{-\gamma^* \cdot t} \right) \\ -c_{21} \cdot \left(e^{-\gamma \cdot t} - e^{-\gamma^* \cdot t} \right) & c_{22} \cdot e^{-\gamma \cdot t} + c_{22}^* \cdot e^{-\gamma^* \cdot t} \end{bmatrix},$$

$$\mathbf{\Phi}(t - \psi) = \begin{bmatrix} c_{11} \cdot e^{-\gamma \cdot (t-\psi)} + c_{11}^* \cdot e^{-\gamma^* \cdot (t-\psi)} & -c_{12} \cdot \left(e^{-\gamma \cdot (t-\psi)} - e^{-\gamma^* \cdot (t-\psi)} \right) \\ -c_{21} \cdot \left(e^{-\gamma \cdot (t-\psi)} - e^{-\gamma^* \cdot (t-\psi)} \right) & c_{22} \cdot e^{-\gamma \cdot (t-\psi)} + c_{22}^* \cdot e^{-\gamma^* \cdot (t-\psi)} \end{bmatrix}$$

(30)

From here, all parameters and constants are defined by:

$$\begin{cases} c_{11} = \dfrac{1}{2} \cdot \left(1 - \left(\dfrac{\alpha \cdot \tau_2 - 1}{\tau_2 \cdot \sqrt{\alpha^2 - \beta^2}} \right) \right) \\ c_{11}^* = \dfrac{1}{2} \cdot \left(1 + \left(\dfrac{\alpha \cdot \tau_2 - 1}{\tau_2 \cdot \sqrt{\alpha^2 - \beta^2}} \right) \right) \\ c_{12} = \dfrac{1}{2} \cdot \dfrac{k_{11}}{\tau_1 \cdot \sqrt{\alpha^2 - \beta^2}} \end{cases}, \quad \begin{cases} c_{21} = \dfrac{1}{2} \cdot \dfrac{k_{21}}{\tau_2 \cdot \sqrt{\alpha^2 - \beta^2}} \\ c_{22} = \dfrac{1}{2} \cdot \left(1 - \left(\dfrac{\alpha \cdot \tau_1 - 1}{\tau_1 \cdot \sqrt{\alpha^2 - \beta^2}} \right) \right) \\ c_{22}^* = \dfrac{1}{2} \cdot \left(1 + \left(\dfrac{\alpha \cdot \tau_1 - 1}{\tau_1 \cdot \sqrt{\alpha^2 - \beta^2}} \right) \right) \\ \gamma = \alpha - \sqrt{\alpha^2 - \beta^2} \\ \gamma^* = \alpha + \sqrt{\alpha^2 - \beta^2} \end{cases}$$

(31)

The parameters α, β, τ_1, and τ_2 are clearly defined as follows:

$$\alpha = \frac{1}{2} \cdot \frac{1}{\tau_1 \| \tau_2}, \quad \beta = \sqrt{\frac{1 - k_{11} \cdot k_{21}}{\tau_1 \cdot \tau_2}}$$

(32)

From here, $\tau_1 \| \tau_2 = \tau_1 \cdot \tau_2 / (\tau_1 + \tau_2)$. After replacing (30) in (22) and simplifying the resulting expression, the dynamic for $v_{C1}(t)$ and $v_{C2}(t)$ can be derived in a compact form given by (33). Also, $i \in \{1, 2\}$. All parameters and constants in (33) are defined by (34). Here $P_{i1} = 1/\tau_i$, $Q_{i1} = k_{i1}/\tau_i$, and $Q_{21} = k_{21}/\tau_2$. It should be noted, that k_{i1}, k_{21}, and τ_i are already defined in

$$v_{C_i}(t) = (C_{i1} \cdot e^{m_{i1} \cdot t} + C_{i2} \cdot e^{m_{i2} \cdot t}) + \left(V_{C_{i1}} \cdot \sin(\omega \cdot t + \sigma_{i1}) + V_{C_{i2}} \cdot \sin(\omega \cdot t + \sigma_{i2}) \right) \tag{33}$$

$$\begin{cases} V_{C_{i1}} = \dfrac{U_{i1}}{\sqrt{m_{i1}^2 + \omega^2}} \\[2mm] V_{C_{i2}} = \dfrac{U_{i2}}{\sqrt{m_{i2}^2 + \omega^2}} \\[2mm] m_{i1} = -\alpha_{i1} + \sqrt{\alpha_{i1}^2 - \beta_{i1}^2} \\[2mm] m_{i2} = -\alpha_{i1} - \sqrt{\alpha_{i1}^2 - \beta_{i1}^2} \end{cases}, \quad \begin{cases} \alpha_{i1} = \dfrac{1}{2} \cdot a_{i1} \\[1mm] \beta_{i1} = \sqrt{b_{i1}} \\[1mm] a_{i1} = P_{11} + P_{21} \\[1mm] b_{i1} = P_{11} \cdot P_{21} - Q_{11} \cdot Q_{21} \\[1mm] \sigma_{i1} = \theta_{i1} + \delta_{i1} \\[1mm] \sigma_{i2} = \theta_{i1} - \delta_{i1} \\[1mm] \theta_{i1} = \tan^{-1}\left(\dfrac{\omega}{m_{i2}}\right) \\[1mm] \varphi_{i1} = \tan^{-1}\left(\dfrac{m_{i2}}{\omega}\right) \\[1mm] \delta_{i1} = \tan^{-1}\left(\dfrac{\omega}{m_{i1}}\right) \end{cases} \tag{34}$$

(11). Integration constants are defined as well, assuming null initial conditions stated as follows:

$$\begin{cases} C_{i1} = -\left(\dfrac{1}{m_{i1} - m_{i2}}\right) \cdot \left(-m_{i2} \cdot V_{C_{i1}} \cdot \sin(\sigma_{i1}) - m_{i2} \cdot V_{C_{i2}} \cdot \sin(\sigma_{i2}) + \right. \\[2mm] \left. \qquad\qquad + \omega \cdot V_{C_{i1}} \cdot \sin(\sigma_{i1}) + \omega \cdot V_{C_{i2}} \cdot \sin(\sigma_{i2}) \right) \\[3mm] C_{i2} = \left(\dfrac{1}{m_{i1} - m_{i2}}\right) \cdot \left(-m_{i1} \cdot V_{C_{i1}} \cdot \sin(\sigma_{i1}) - m_{i1} \cdot V_{C_{i2}} \cdot \sin(\sigma_{i2}) + \right. \\[2mm] \left. \qquad\qquad + \omega \cdot V_{C_{i2}} \cdot \sin(\sigma_{i1}) + \omega \cdot V_{C_{i1}} \cdot \sin(\sigma_{i2}) \right) \end{cases} \tag{35}$$

The output voltage $v_o(t)$ is then obtained by substituting the result of (33) into (5). Equation (35) provides a detailed account of the voltage dynamics $v_{Ci}(t)$, including both exponential decay terms and sinusoidal components that reflect the transient and oscillatory behavior of the system. The amplitudes V_{Ci1} and V_{Ci2} of the sinusoidal terms are determined by U_{i1} and U_{i2}, respectively, and are influenced by the frequencies and decay rates m_{i1} and m_{i2}. The decay rates are calculated using the constants α_{i1} and β_{i1}, which depend on the parameters a_{i1}, b_{i1}, P_{11}, and P_{21}. The phase angles σ_{i1} and σ_{i2} are determined by θ_{i1}, φ_{i1}, and δ_{i1}, reflecting the relationship between frequency and decay rate. Additionally, the integration constants C_{i1} and C_{i2} account for the system's initial conditions, ensuring a smooth transition from transient to steady-state behavior. Overall, (34) provides a comprehensive framework for understanding the time evolution of $v_{Ci}(t)$, capturing both transient and oscillatory phenomena in a complex yet interpretable manner.

4.4. Solution of the CCA high frequency small signal model

The matrix $\mathbf{\Phi}(t)$, which is related to the matrix $\mathbf{A}$ defined in (13), is defined as:

$$\mathbf{\Phi}(t) = \begin{bmatrix} e^{-\frac{t}{\tau_1}} & 0 \\[2mm] c \cdot \left(e^{-\frac{t}{\tau_2}} - e^{-\frac{t}{\tau_1}} \right) & e^{-\frac{t}{\tau_2}} \end{bmatrix}, \quad \mathbf{\Phi}(t - \psi) = \begin{bmatrix} e^{-\frac{t-\psi}{\tau_1}} & 0 \\[2mm] c \cdot \left(e^{-\frac{t-\psi}{\tau_2}} - e^{-\frac{t-\psi}{\tau_1}} \right) & e^{-\frac{t-\psi}{\tau_2}} \end{bmatrix} \tag{36}$$

where $c = k_{22} \cdot \tau_1 / (\tau_1 - \tau_2)$ and k_{22}, τ_1, and τ_2 are defined in (14). After substituting (36) into (22) and performing some algebraic manipulations, the expressions of the SVs associated with this model are described as follows:

$$
\begin{cases}
v_{C_{b'e}}(t) = \dfrac{Q_{11}}{\sqrt{P_{11}^2 + \omega^2}} \cdot (\sin(\omega \cdot t - \theta) + \sin(\theta) \cdot e^{-P_{11} \cdot t}) \\[3ex]
v_{C_L}(t) = \dfrac{Q_{21}}{\sqrt{P_{21}^2 + \omega^2}} \cdot (\sin(\omega \cdot t - \varphi) + \sin(\varphi) \cdot e^{-P_{22} \cdot t}) - \\[3ex]
\quad - \dfrac{Q_{11} \cdot Q_{22}}{\sqrt{P_{11}^2 + \omega^2} \cdot \sqrt{P_{21}^2 + \omega^2}} \cdot (\sin(\omega \cdot t - \delta) + \sin(\delta) \cdot e^{-P_{22} \cdot t}) - \\[3ex]
\quad - \dfrac{Q_{11} \cdot Q_{22}}{\sqrt{P_{11}^2 + \omega^2} \cdot (P_{21} - P_{11})} \cdot \sin(\theta) \cdot (e^{-P_{11} \cdot t} - e^{-P_{21} \cdot t})
\end{cases}
\tag{37}
$$

The constants $P_{i1} = 1/\tau_i$, $Q_{i1} = k_{i1} \cdot V/\tau_i$, $Q_{22} = k_{22}/\tau_2$, and $j = \text{atan}(\omega/P_{i1})$, $\delta = \theta + \phi$, where $j \in \{\theta, \phi\}$ and $i \in \{1, 2\}$.

Equation (37) clearly describes the voltage dynamics across the base-emitter capacitance ($v_{C_{b'e}}(t)$) and the load capacitance ($v_{C_L}(t)$) in a transistor amplifier circuit under sinusoidal excitation. This equation provides a comprehensive understanding of the circuit's behavior and can be used to make informed design decisions with confidence. The constants Q_{11}, Q_{21}, and Q_{22} represent the amplitudes of sinusoidal components, while P_{11} and P_{21} are inversely related to time constants (τ_i ($i \in \{1, 2\}$)) governing the exponential decay rates of these components. The angular frequency determines the frequency of the sinusoidal waveform, while the phase angles θ and ϕ denote the phase relationships. The equation incorporates the interplay between exponential decay terms, sinusoidal components, and phase relationships, offering insights into both transient behavior and steady-state response characteristics of the transistor amplifier circuit under sinusoidal state.

4.5. Solution of the CBA low frequency small signal model

Considering the matrix $\mathbf{A}$ defined in (15), the $\mathbf{\Phi}(t)$ is derived by (24), which is defined as follows:

$$
\mathbf{\Phi}(t) = \begin{bmatrix} e^{-\frac{t}{\tau_1}} & 0 \\ -c \cdot \left(1 - e^{-\frac{t}{\tau_1}}\right) & 1 \end{bmatrix}, \quad
\mathbf{\Phi}(t - \psi) = \begin{bmatrix} e^{-\frac{t-\psi}{\tau_1}} & 0 \\ -c \cdot \left(1 - e^{-\frac{t-\psi}{\tau_1}}\right) & 1 \end{bmatrix}
\tag{38}
$$

From here, $c = k_{21} \cdot \tau_1/\tau_2$ and k_{21}, τ_1, and τ_2 are already defined in (16). After replacing (38) in (22) and simplifying the dynamic expressions of the SVs, $v_{C1}(t)$ and $v_{C2}(t)$ are obtained and defined as follows:

$$
\begin{cases}
v_{C_1}(t) = \dfrac{Q_{11}}{\sqrt{P_{11}^2 + \omega^2}} \cdot (\sin(\omega \cdot t - \theta) + \sin(\theta) \cdot e^{-P_{11} \cdot t}) \\[3ex]
v_{C_2}(t) = \dfrac{Q_{21}}{\omega} \cdot \left(\cos(\omega \cdot t - \theta) - \cos(\theta)\right) - \dfrac{Q_{22}}{P_{11}} \cdot (1 - e^{-P_{11} \cdot t}) + \dfrac{Q_{23}}{\omega} \cdot (1 - \cos(\omega \cdot t))
\end{cases}
\tag{39}
$$

where $P_{11} = 1/\tau_1$, $Q_{11} = V \cdot P_{11}$, $Q_{21} = k_{21} \cdot Q_{11}/(\tau_2 \cdot \text{sqrt}(P_{11}^2 + \omega^2))$, $Q_{22} = k_{21} \cdot \sin(\theta)/\tau_2$, and $Q_{23} = k_{21} \cdot V/\tau_2$. On the other hands, $\theta = \text{atan}(\omega/P_{11})$. As with previous cases, replacing (39) in (5) yields the voltage $v_o(t)$.

The equation provided (39) describes the time-dependent behavior of voltage across two capacitances, $v_{C1}(t)$ and $v_{C2}(t)$, within a circuit. Each capacitance exhibits distinct dynamics. $v_{C1}(t)$ is governed by a sinusoidal term modulated by an exponential decay factor. This reflects both the sinusoidal excitation at angular frequency and the transient response

characterized by the decay constant P_{11}. The amplitude Q_{11} signifies the magnitude of the sinusoidal component, while θ represents the phase angle. Similarly, $v_{C2}(t)$ is expressed as a combination of sinusoidal and exponential terms, illustrating a more complex response. The first term represents the sinusoidal contribution, while the subsequent terms involve exponential decay and frequency-dependent components, reflecting the interplay of transient and steady-state effects. The amplitudes and relationships between these components are dictated by constants such as Q_{21}, Q_{22}, and Q_{23}, capturing the intricate dynamics of the circuit. This equation offers valuable insights into the transient and steady-state behavior of the circuit when subjected to sinusoidal excitation, providing a comprehensive understanding of its response characteristics.

4.6. Solution of the CBA high frequency small signal model

Using the matrix **A** defined in (17), the $\mathbf{\Phi}(t)$ is derived by (24), which is given by:

$$\mathbf{\Phi}(t) = \begin{bmatrix} e^{-\frac{t}{\tau_1}} & 0 \\ -c \cdot \left(e^{-\frac{t}{\tau_1}} - e^{-\frac{t}{\tau_2}} \right) & e^{\frac{t}{\tau_2}} \end{bmatrix}, \ \mathbf{\Phi}(t-\psi) = \begin{bmatrix} e^{-\frac{t-\psi}{\tau_1}} & 0 \\ -c \cdot \left(e^{-\frac{t-\psi}{\tau_1}} - e^{\frac{t-\psi}{\tau_2}} \right) & e^{\frac{t-\psi}{\tau_2}} \end{bmatrix} \quad (40)$$

From here, $c = k_{21} \cdot \tau_1 / (\tau_1 + \tau_2)$ where k_{21}, τ_1 and τ_2 are already defined in (18). After replacing (40) in (22) and performing certain algebraic simplifications, the expressions of the SVs $v_{Cb'e}(t)$ and $v_o(t)$ are given by:

$$\begin{cases} v_{Cb'e}(t) = \dfrac{Q_{11}}{\sqrt{P_{11}{}^2 + \omega^2}} \cdot (\sin(\omega \cdot t - \theta) + \sin(\theta) \cdot e^{-P_{11} \cdot t}) \\ v_o(t) = \dfrac{Q_{21}}{\sqrt{P_{21}{}^2 + \omega^2}} \cdot (\sin(\omega \cdot t - \delta) + \sin(\delta) \cdot e^{-P_{21} \cdot t}) + \dfrac{Q_{22}}{P_{21} - P_{11}} \cdot (e^{-P_{11} \cdot t} - e^{-P_{21} \cdot t}) \end{cases} \quad (41)$$

Also, $P_{i1} = 1/\tau_i$, $Q_{11} = k_{11} \cdot V / \tau_1$, $Q_{21} = k_{21} \cdot Q_{11} / (\tau_2 \cdot \mathrm{sqrt}(P_{11}{}^2 + \omega^2))$, $Q_{22} = Q_{21} \cdot \sin(\theta)$. Also, $j = \mathrm{atan}(\omega / P_{i1})$ and $\delta = \theta + \phi$, where $j \in \{\theta, \phi\}$ and $i \in \{1, 2\}$. Once again, by replacing (41) in (5), the voltage $v_o(t)$ is obtained.

The equation (41) presented delineates the temporal evolution of voltage across two capacitances, $v_{Cb'e}(t)$ and $v_o(t)$, within a circuit subjected to sinusoidal excitation. $v_{Cb'e}(t)$ exhibits sinusoidal modulation compounded with an exponential decay term, encapsulating both the sinusoidal excitation at angular frequency and the transient response characterized by the decay constant P_{11}. The amplitude Q_{11} represents the magnitude of the sinusoidal component, while θ denotes the phase angle. On the other hand, $v_o(t)$ comprises a combination of sinusoidal and exponential terms, reflecting a nuanced response. The sinusoidal term depicts the steady-state contribution, while the exponential terms capture the transient behavior. Constants such as Q_{21} and Q_{22} dictate the amplitudes and interplay between these components, embodying the intricate dynamics of the circuit. Furthermore, δ represents the phase difference between $v_{Cb'e}(t)$ and $v_o(t)$, adding to the complexity of the system's response. By elucidating the temporal dynamics under sinusoidal excitation, this equation offers profound insights into the circuit's transient and steady-state behavior, enriching our comprehension of its response characteristics.

This technical section on the solution of the dynamic and state equations of BJT amplifiers provides a thorough analysis of the equations that govern amplifier behavior across low and high-frequency operational ranges. This section emphasizes the importance of understanding these equations for optimizing design conditions in amplifier circuits, laying the foundation for a detailed exploration. The text systematically presents the methodology for solving the state equations. Various techniques, such as integration factors and Laplace transforms, are employed with a notable emphasis on utilizing the state transition matrix for simplification purposes. The section provides explicit solutions for the SVs in both low and high-frequency models, offering insights into transient and steady-state behaviors under diverse operational conditions.

Each solution is accompanied by an analysis, elucidating the role of parameters like decay rates, amplitudes, and phase angles in shaping the system's dynamics. The section covers various BJT amplifier models and provides a comprehensive understanding of different operational scenarios. It achieves clarity through well-structured equations, clear explanations, and appropriate use of mathematical symbols and terminology. The conclusion concisely summarizes the key findings and emphasizes the practical implications of the derived equations for engineering applications, particularly in circuit design and analysis. Overall, this section provides a comprehensive and informative resource for engineers and researchers interested in exploring BJT amplifier dynamics.

The time expressions of the SVs as a function of the BJT-Amps for the analyzed frequency ranges are summarized in Table 2.

Table 2. Time expressions of the state variables as a function of the BJT-amps topologies.

BJT-Amps	Frequency range	Time-domain state-variable expressions
CEA	Low frequency	$v_{C_1}(t) = \dfrac{Q_{11}}{\sqrt{P_{11}^2 + \omega^2}} \cdot (\sin(\omega \cdot t - \theta) + \sin(\theta) \cdot e^{-P_{11} \cdot t})$
		$v_{C_2}(t) = \dfrac{Q_{21}}{\sqrt{P_{21}^2 + \omega^2}} \cdot (\sin(\omega \cdot t - \varphi) + \sin(\varphi) \cdot e^{-P_{21} \cdot t}) -$
		$- \dfrac{Q_{22}}{\sqrt{P_{21}^2 + \omega^2}} \cdot (\sin(\omega \cdot t - \delta) + \sin(\delta) \cdot e^{-P_{21} \cdot t}) - \dfrac{Q_{23}}{\sqrt{P_{21} + P_{11}}} \cdot (e^{-P_{11} \cdot t} - e^{-P_{21} \cdot t})$
	High frequency	$v_{b'e}(t) = \dfrac{Q_{11}}{\sqrt{P_{11}^2 + \omega^2}} \cdot (\sin(\omega \cdot t - \theta) + \sin(\theta) \cdot e^{-P_{11} \cdot t})$
CCA	Low frequency	$v_{C_i}(t) = (C_{i1} \cdot e^{m_{i1} \cdot t} + C_{i2} \cdot e^{m_{i2} \cdot t}) + \left(V_{C_{i_1}} \cdot \sin(\omega \cdot t + \sigma_{i1}) + V_{C_{i_2}} \cdot \sin(\omega \cdot t + \sigma_{i2}) \right), \forall i \in \{1,2\}$
	High frequency	$v_{C_{b'e}}(t) = \dfrac{Q_{11}}{\sqrt{P_{11}^2 + \omega^2}} \cdot (\sin(\omega \cdot t - \theta) + \sin(\theta) \cdot e^{-P_{11} \cdot t})$
		$v_{C_L}(t) = \dfrac{Q_{21}}{\sqrt{P_{21}^2 + \omega^2}} \cdot (\sin(\omega \cdot t - \varphi) + \sin(\varphi) \cdot e^{-P_{22} \cdot t}) - \dfrac{Q_{11} \cdot Q_{22}}{\sqrt{P_{11}^2 + \omega^2} \cdot \sqrt{P_{21}^2 + \omega^2}} \cdot (\sin(\omega \cdot t - \delta) + \sin(\delta) \cdot e^{-P_{22} \cdot t}) -$
		$- \dfrac{Q_{11} \cdot Q_{22}}{\sqrt{P_{11}^2 + \omega^2} \cdot (P_{21} - P_{11})} \cdot \sin(\theta) \cdot (e^{-P_{11} \cdot t} - e^{-P_{21} \cdot t})$
CBA	Low frequency	$v_{C_1}(t) = \dfrac{Q_{11}}{\sqrt{P_{11}^2 + \omega^2}} \cdot (\sin(\omega \cdot t - \theta) + \sin(\theta) \cdot e^{-P_{11} \cdot t})$
		$v_{C_2}(t) = \dfrac{Q_{21}}{\omega} \cdot \left(\cos(\omega \cdot t - \theta) - \cos(\theta) \right) - \dfrac{Q_{22}}{P_{11}} \cdot (1 - e^{-P_{11} \cdot t}) + \dfrac{Q_{23}}{\omega} \cdot \left(1 - \cos(\omega \cdot t) \right)$
	High frequency	$v_{C_{b'e}}(t) = \dfrac{Q_{11}}{\sqrt{P_{11}^2 + \omega^2}} \cdot (\sin(\omega \cdot t - \theta) + \sin(\theta) \cdot e^{-P_{11} \cdot t})$
		$v_o(t) = \dfrac{Q_{21}}{\sqrt{P_{21}^2 + \omega^2}} \cdot (\sin(\omega \cdot t - \delta) + \sin(\delta) \cdot e^{-P_{21} \cdot t}) + \dfrac{Q_{22}}{P_{21} - P_{11}} \cdot (e^{-P_{11} \cdot t} - e^{-P_{21} \cdot t})$

5. Simulation results

This section presents simulation results for the dynamic models of the three BJT-Amps topologies (CEA, CCA, and CBA) under transient conditions, valid for both low and high frequencies. The simulations have been carried out using

MATLAB-Simulink.

5.1. CEA simulation results

Tables 3 and 4 summarize the simulation parameters for low and high frequency operation of the CEA, respectively. For the low-frequency model, a voltage-wave current source with a peak-to-peak value of 5 mV at a frequency of 10 Hz and an internal resistance of 1 mΩ is assumed. For the high-frequency model, the same voltage source used in the low-frequency case is considered, but with an operating frequency of 100 MHz. Additionally, for all BJT-Amps cases, V_T is assumed to be 26 mV.

Figure 9 shows the steady-state dynamics of the low-frequency CEA model. The figure corresponds to the output of both the simulation model in Simulink, labeled $v_{\mathrm{osimulink}}(t)$, and the analytical solution $v_\mathrm{o}(t)$ extracted from (5). The dynamics of both variables are identical, indicating a negligible error and confirming the validity of the solution obtained in (26).

The gain generated by this amplifier is notably high, with a measured value of $|A_\mathrm{v}| \approx 1,740$. While the transistor's dc current gain is set to $\beta = 200$, this does not directly limit the voltage gain. The high voltage gain arises from the combination
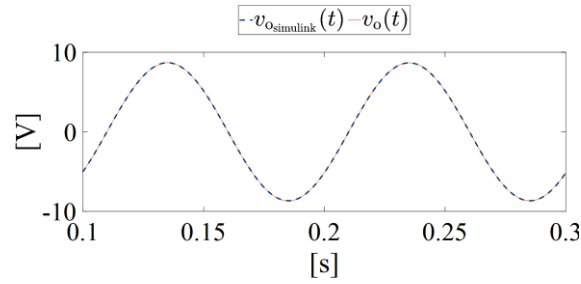

Figure 9. Simulation results of $v_{\mathrm{osimulink}}(t)$ and $v_\mathrm{o}(t)$ in steady state when the CEA operates at low frequency. Initial conditions are zero.

Table 3. Simulation parameters for CEA for low frequencies.

Parameter	Value
R_b	1.0 [kΩ]
R_c	1.5 [kΩ]
R_e	200 [Ω]
R_L	100 [Ω]
r_{C1}	1 [mΩ]
r_{C2}	1 [mΩ]
C_1	20 [μF]
C_2	20 [μF]
hie	1 [kΩ]
β	200

Table 4. Simulation parameters for CEA for high frequencies.

Parameter	Value
R_b	2.0 [kΩ]
R_c	1.5 [kΩ]
R_L	200 [Ω]
$C_{b'c}$	2 [pF]
$C_{b'e}$	200 [pF]

of a large transconductance $g_m = I_C/V_T$ and a high effective load resistance in the simulation setup. These conditions, along with the small input signal amplitude and optimized biasing, result in a significantly amplified output. This behavior is consistent with theoretical expectations and supports findings in the literature [19–21].

Figure 10 describes the steady-state dynamics of $v_o(t)$ from the Simulink model ($v_{osimulink}(t)$) and from (9) labeled $v_o(t)$. These dynamics are valid for the CEA system at high frequency. As shown in Figure 9, the two dynamics are very similar, verifying a negligible error (24 µV) and confirming that the solution in (29) is appropriate. The voltage gain for this system is $|A_v| \approx 259$. The Miller capacitance causes a decrease in gain compared to when the amplifier operates at low frequency [19–21].

5.2. CCA simulation results

Table 5 and Table 6 provide the simulation parameters of the CCA when operating at low and high frequencies, respectively.

For the low-frequency model, a voltage-wave current source with a peak-to-peak value of 5 mV at a frequency of 10 Hz and an internal resistance of 1 mΩ is assumed. For the high-frequency model, the same voltage source used in the low-frequency case is considered, but with an operating frequency of 100 MHz.

Figure 11 shows the steady-state variable $v_o(t)$ in the form of $v_{osimulink}(t)$ from the simulation model and $v_o(t)$ extracted from (33). It is evident that both variables share the same dynamics, verifying that their error is zero. Additionally, it can be observed that the voltage gain is less than one in the low- frequency case [20], i.e., $|A_v| = 4 \cdot 10^{-4}$. This very low gain reflects the dc behavior of the circuit, where coupling capacitors block the signal path. In contrast, the dynamic gain observed in transient simulations ($A_v \approx 1.25$) reflects the ac response under sinusoidal excitation. While this value slightly
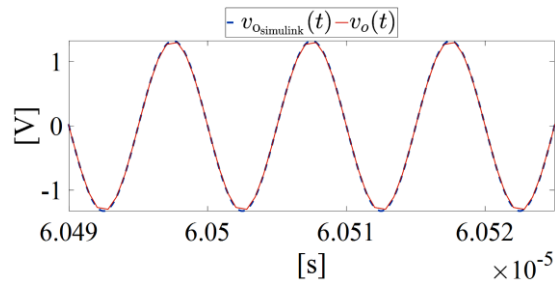
Figure 10. Simulation results of $v_{osimulink}(t)$ and $v_o(t)$ in steady-state when the CEA operates at high frequency. Initial conditions are zero.

Table 5. Simulation parameters for CCA for low frequencies.

Parameter	Value
R_1	20 [kΩ]
R_2	2 [kΩ]
R_E	50 [Ω]
R_L	100 [Ω]
C_1	100 [μΩ]
C_2	3.3 [μΩ]
r_{C1}	1 [mΩ]
r_{C2}	1 [mΩ]
V_{BE}	0.7 [V]
V_{CC}	20 [V]
$β$	200

Table 6. Simulation parameters for CCA for high frequencies.

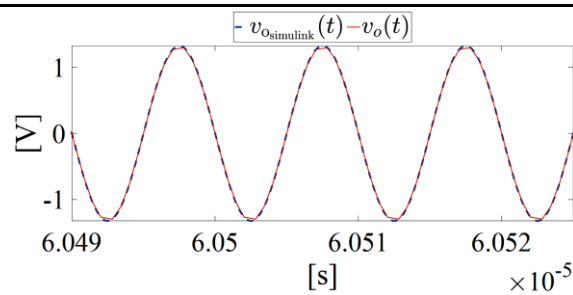| Parameter	Value
R_b	2 [kΩ]
R_L	100 [Ω]
$C_{b'c}$	10 [pF]
$C_{b'e}$	100 [pF]
C_L	100 [μF]
r_{CL}	100 [mΩ]

Figure 11. Simulation results of $v_{o_{simulink}}(t)$ and $v_o(t)$ in steady-state when the CCA operates in low frequency. Initial conditions are zero.

exceeds unity, it is consistent with simulation conditions and does not contradict the theoretical behavior of the emitter

follower, which ideally has a voltage gain slightly less than 1 due to the base- emitter voltage drop.

Figure 12 shows the dynamics of $v_{\text{osimulink}}(t)$ extracted directly from the Simulink model and $v_\text{o}(t)$ modeled by (5). Both waveforms exhibit identical dynamics, validating the correct solution of the system shown in (37).

The voltage gain for this system is $|A_\text{v}| = 1.25$, which is consistent with the literature [19], suggesting an $|A_\text{v}|$ close to unity.

For the low-frequency model, a sine-wave voltage source with a peak-to-peak value of 10 mV at a frequency of 10 kHz and an internal resistance of 50 Ω is assumed. For the high-frequency model, the same voltage source used in the low-frequency case is considered, but with an operating frequency of 10 MHz.

Table 7 and Table 8 provide the simulation parameters of the CBA when operating at low and high frequencies, respectively.

Figure 13 shows the steady-state voltages of $v_{\text{osimulink}}(t)$ from the Simulink simulation model and $v_\text{o}(t)$ modeled by (5).

The dynamics can be verified by checking the correctness of the expressions in (41). Additionally, $|Av| \approx 1.42$, which is slightly larger than 1, but smaller than in the CEA case [19,20].

In Figure 14 the variables $v_{\text{osimulink}}(t)$ and $v_\text{o}(t)$ are shown, where the former is extracted directly from the simulation model and the latter comes from (5). It is evident that both dynamics share the same form, which again verifies that the solutions of this dynamic model defined in (41) are proper. Additionally, the voltage gain $|Av|$ is 252, which is higher than the $|Av|$ of the CCA [20].

This section presents the simulation results of three BJT-Amps topologies: CEA, CCA, and CBA, under transient conditions for both low and high frequencies. The simulations were conducted using MATLAB-Simulink to examine the behavior of these amplifiers. The simulation parameters for both low and high frequency operations are summarized in tables for the CEA. The low-frequency model assumes a voltage-wave current source, while the high-frequency model assumes a similar source but with a higher operating frequency. Figures are used to illustrate the steady-state frequency. Figures are used to illustrate the steady-state dynamics of the CEA model, validating the solutions obtained and demonstrating a high gain, which is consistent with literature findings. Similar analyses were conducted for the CCA and CBA. Tables outlining simulation parameters and figures depicting steady- state dynamics were included. These simulations confirmed the accuracy of the models and highlighted differences in voltage gain between low and high frequencies, providing valuable insights into the performance of each amplifier topology.

While SPICE-based simulators are standard tools for circuit analysis, this study employs MATLAB-Simulink due to its strengths in state-space modeling, time-domain simulation, and system-level analysis. Simulink's visual modeling environment and native support for dynamic systems make it particularly suitable for exploring the transient behavior of BJT amplifiers across frequency domains, which is the focus of this work.
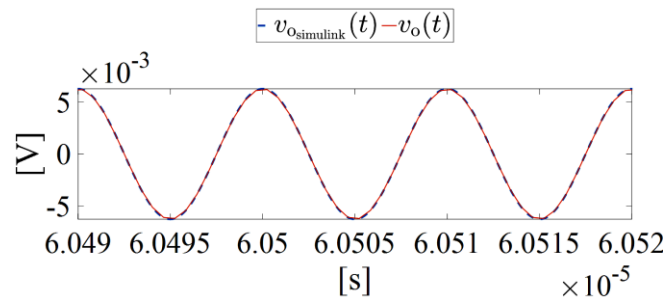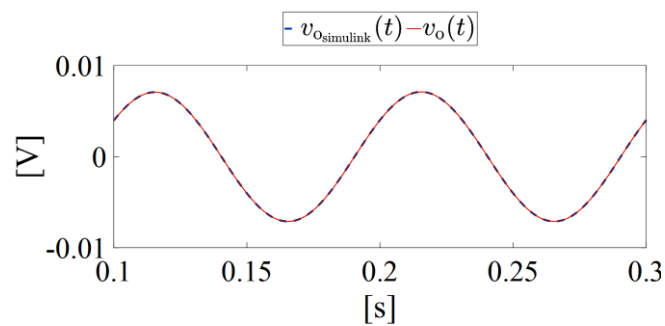

Figure 12. Simulation results of $v_{\text{osimulink}}(t)$ and $v_\text{o}(t)$ in steady-state when the CCA operates at high frequency. Initial conditions are zero.

Table 7. Simulation parameters for CBA for low frequencies

Parameter	Value
R_L	20 [kΩ]
C_1	200 [μF]
C_2	10 [μF]
r_{C1}	1 [mΩ]
r_{C2}	1 [mΩ]
hfb	200
hib	16
V_{BE}	0.7 [V]
V_{CC}	20 [V]
β	20

Table 8. Simulation parameters for CBA for high frequencies.

Parameter	Value
$C_{b'e'}$	5.5 [nF]
$C_{b'c'}$	4 [pF]
R_L	100 [Ω]
$r_{be'}$	12.5 [Ω]

Figure 13. Simulation results of $v_{o\text{simulink}}(t)$ and $v_o(t)$ in steady-state when the CBA operates in low frequency. Initial conditions are zero.
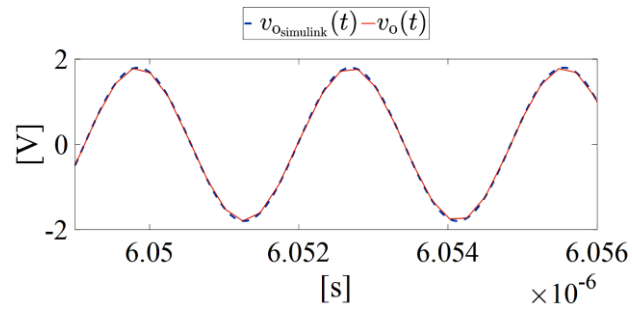
Figure 14. Simulation results of $v_{o_{simulink}}(t)$ and $v_o(t)$ in steady-state when the CBA operates in high frequency. Initial conditions are zero.

6. Conclusion

The analysis of three bipolar-junction-transistor amplifier topologies, namely common-emitter amplifier, common-collector amplifier, and common-base amplifier, under transient conditions, covering both low and high frequencies, provides valuable insights into their operational behavior and performance characteristics. MATLAB-Simulink simulations were used to examine each topology's response to varying frequency inputs, revealing their suitability for diverse applications. The models at low frequency, characterized by voltage or current sources with specific parameters, enabled a detailed investigation into the steady-state dynamics of output variables. The common-emitter amplifier topology demonstrated high gains, which is consistent with established literature findings. On the other hand, the common-collector amplifier, and collector-base amplifier topologies exhibited lower gains, with slight variations between them. Transitioning to high-frequency operation revealed the impact of Miller capacitance on gain reduction, especially in the common-emitter amplifier topology. However, all topologies remained functional, and their respective models were validated through simulations. The simulation parameters were meticulously adjusted for each frequency range, facilitating an accurate representation of real-world scenarios. These findings emphasize the significance of comprehending amplifier behavior across frequency domains, providing valuable insights for engineers designing circuits for various applications. The study contributes to the broader understanding of bipolar-junction-transistor amplifier performance under transient conditions, aiding in the informed selection and design of amplifier configurations based on and demonstrating a high gain, which is consistent with literature findings. Similar analyses were conducted for the CCA and CBA. Tables outlining simulation parameters and figures depicting steady-state dynamics were included. These specific application requirements and frequency considerations.

Conflict of Interest

There is no conflict of interest for this study.

References

[1]   Perez-Verdu, B.; Huertas, J.L.; Rodriguez-Vazquez, A. A New Nonlinear Time-Domain Op-Amp Macromodel Using Threshold Functions and Digitally Controlled Network Elements. *IEEE Journal of Solid-State Circuits* **1988**, *23*, 959–971, doi:10.1109/4.347.

[2] Bowers, D.F. A Fast Precision Operational Amplifier Featuring Two Separate Control Loops. In Proceedings of the 2014 IEEE Bipolar/BiCMOS Circuits and Technology Meeting (BCTM); September 2014; pp. 72–75.

[3] Gilasgar, M.; Barlabé, A.; Pradell, L. High-Efficiency Reconfigurable Dual-Band Class-F Power Amplifier With Harmonic Control Network Using MEMS. *IEEE Microwave and Wireless Components Letters* **2020**, *30*, 677–680, doi:10.1109/LMWC.2020.2994373.

[4] Hosseini, S.E.; Dehrizi, H.G. A New BJT-Transistor with Ability of Controlling Current Gain. In Proceedings of the International Multi-Conference on Systems, Signals & Devices; March 2012; pp. 1–4.

[5] De Langen, K.-J.; Huijsing, J.H. Compact Low-Voltage Power-Efficient Operational Amplifier Cells for VLSI. *IEEE Journal of Solid-State Circuits* **1998**, *33*, 1482–1496, doi:10.1109/4.720394.

[6] Kong, L.; Liu, H.; Zhu, X.; Boon, C.C.; Li, C.; Liu, Z.; Yeo, K.S. Design of a Wideband Variable-Gain Amplifier With Self-Compensated Transistor for Accurate dB-Linear Characteristic in 65 Nm CMOS Technology. *IEEE Transactions on Circuits and Systems I: Regular Papers* **2020**, *67*, 4187–4198, doi:10.1109/TCSI.2020.2995725.

[7] Pandiev, I.M.; Stoimenov, E.Ch. Development of Single-Transistor Amplifier Modular Laboratory Kits for Electronic Engineering Education. In Proceedings of the 2020 XI National Conference with International Participation (ELECTRONICA); July 2020; pp. 1–4.

[8] Farag, F.A.; Khalaf, Y.A. Digitally-Controlled Variable-Gain-Amplifier Based on Current Conveyor with Opamp and Inverters Only. In Proceedings of the 2010 International Conference on Microelectronics; December 2010; pp. 224–227.

[9] Makarov, D.G.; Kryzhanovskyi, V.V.; Krizhanovski, V.G.; Grebennikov, A.V. Experimental Investigation of Class E Power Amplifier with Shunt Filter for Reduced Duty Ratio. In Proceedings of the 2018 International Conference on Information and Telecommunication Technologies and Radio Electronics (UkrMiCo); September 2018; pp. 1–4.

[10] Nam, H.; Nguyen, D.-A.; Kim, Y.; Seo, C. Design of 6 GHz Variable-Gain Low-Noise Amplifier Using Adaptive Bias Circuit for Radar Receiver Front End. *Electronics* **2023**, *12*, 2036, doi:10.3390/electronics12092036.

[11] Rode, D.L. Output Resistance of the Common–Emitter Amplifier. *IEEE Trans. Electron Devices* **2005**, *52*, 2004–2008, doi:10.1109/TED.2005.854277.

[12] Sivonen, P.; Kangasmaa, S.; Parssinen, A. Analysis of Packaging Effects and Optimization in Inductively Degenerated Common-Emitter Low-Noise Amplifiers. *IEEE Trans. Microwave Theory Techn.* **2003**, *51*, 1220–1226, doi:10.1109/TMTT.2003.809633.

[13] Ozeren, E.; Cahskan, C.; Davulcu, M.; Kayahan, H.; Gurbuz, Y. 4-Bit SiGe Phase Shifter Using Distributed Active Switches and Variable Gain Amplifier for X-Band Phased Array Applications. In Proceedings of the 2014 9th European Microwave Integrated Circuit Conference; IEEE: Rome, October 2014; pp. 257–260.

[14] Um, J.-Y. A Compact Variable Gain Amplifier With Continuous Time-Gain Compensation Using Systematic Predistorted Gain Control. *IEEE Trans. Circuits Syst. II* **2022**, *69*, 274–278, doi:10.1109/TCSII.2021.3090424.

[15] Bandler, J.W.; Biernacki, R.M.; Cai, Q.; Chen, S.H. Compression Analysis of a High Power BJT Amplifier. In Proceedings of the Third International Workshop on Integrated Nonlinear Microwave and Millimeterwave Circuits; October 1994; pp. 173–178.

[16] Hashem, M.A. Analysis and Design of BJT Differential Amplifier. In Proceedings of the 2022 5th International Conference on Engineering Technology and its Applications (IICETA); May 2022; pp. 227–232.

[17] Liu, Y.; Hiblot, G.; Furuhashi, T.; Lin, H.; Velenis, D.; De Wolf, I. Study of Out-of-Plane Mechanical Stress Impact on Si BJT and Diffusion Resistor Using in-Situ Nanoindentation Probing. *Microelectronics Reliability* **2019**, *100–101*, 113367, doi:10.1016/j.microrel.2019.06.059.

[18] Santos, L.A.P. An Overview on Bipolar Junction Transistor as a Sensor for X-Ray Beams Used in Medical Diagnosis. *Sensors* **2022**, *22*, 1923, doi:10.3390/s22051923.

[19] Savant, C.J.; Roden, M.S.; Carpenter, G.L. *Electronic Design: Circuits and Systems*; Subsequent edition.; Benjamin-

Cummings Pub Co: Redwood City, Calif, 1990; ISBN 978-0-8053-0285-1.

[20] Schilling, D.L. *Electronic Circuits: Discrete and Integrated*;

[21] Sedra, A.S.; Smith, K.C. *Microelectronic Circuits*; Oxford University Press, 2004; ISBN 978-0-19-514252-5.

[22] Stupelman, V.; Filaretov, G.I.; Ivanov,   transtated from the R. by P. *Semiconductor Devices*; Mir Publishers, 1981;

[23] Schubert Jr., T.F.; Kim, E.M. A Short Study on the Validity of Miller's Theorem Applied to Transistor Amplifier High-Frequency Performance. *IEEE Transactions on Education* **2009**, *52*, 92–98, doi:10.1109/TE.2008.919808.

[24] Hayatee, F. The Equivalent Series Resistance in Electrolytic Capacitors. *Active and Passive Electronic Components* **1975**, *2*, doi:10.1155/APEC.2.67.

[25] Cheng, D.K. *Analysis of Linear Systems*; First Edition.; Addison Wesley Publishing Co: Reading, Mass., 1959; ISBN 978-0-201-01020-6.

[26] Katsuhiko, O. *Modern Control Engineering*; Boston, 2009; ISBN 978-0-13-615673-4.

[27] Kuo, B.C. *Automatic Control Systems*; 6th edition.; Prentice Hall: Englewood Cliffs, N.J, 1991; ISBN 978-0-13-051046-4.

[28] Brogan, W.L. *Modern Control Theory*; Prentice Hall, 1991; ISBN 978-0-13-589763-8.